Solid-state nanopore and nanostructure for biomolecule detection

Young Wook Chang

The Graduate School

Yonsei University

Graduate Program for Nanomedical Science

Solid-state nanopore and nanostructure for biomolecule detection

Supervisor: Kyung-Hwa Yoo

A Dissertation

Submitted to the Graduate School of Yonsei University

in partial fulfillment of the

requirements for the degree of

Doctor of philosophy

January 2013

Young Wook Chang

This certifies that the dissertation thesis of
Young Wook Chang is approved.

_____
Thesis Supervisor: Kyung-Hwa Yoo

_____
Thesis Committee Member : Dug Young Kim

_____
Thesis Committee Member : Jae-Chul Pyun

_____
Thesis Committee Member : Donghyun Kim

_____
Thesis Committee Member : Chi Won Ahn

The Graduate School
Yonsei University
January 2013

CONTENTS

LIST OF FIGURES

ABSTRACT

Solid-state nanopore and nanostructure for biomolecule detection

Young Wook Chang

In this thesis, we present the main aspects involved in the small molecule detection based on the nanotechnology - nanopore, carbon nanotube Field-effect Transistors (CNT-FETs), and the Giant Magnetoresitance (GMR) device using ferromagnetic nanowire heterostructures. The first part of this thesis deals with the nanotechnology, DNA, proteins, nanopores, ions, and much more. In that chapter, we first zoom in on the nanoscale and describe the biological context for the experimental work described here. Part of this thesis is devoted to the studying aspects of bare λ- and ladder DNA both for example, how the effective charge of DNA is affected by the presence of various ions. This sensor, known as a solid-state nanopore, consists of a tiny hole that is drilled in a thin solid material with a

focused electron beam. Another part of this thesis is devoted to the development of a biosensor for protein and DNA modified Au nanoparticles using nanocapillary, designed for ease of fabrication, a novel type of nanopore alternatives, fabricated by heating and pulling the crystal or amorphorous SiO_2 tube. The sane electrophoretic events were observed for various molecules, and the series of experimental, theoretical approaches applied for solid-state nanopore were applicable with this platform, confirming the availability of nanocapillary instruments. In the middle part of this thesis, another nanostructure , known as CNT, was exploited for gas molecule detection and it was shown that how this interacts with various molecules electrically, resulting in concentration determination, explained with typical FET scheme, where gas molecules act as gate field source and CNT corresponds to p-type semiconducting channel. Lastly, nanowire type structure was fabricated for GMR effect, where ferromagnetic heterostructure was grown electrochemically inside the Anodized Aluminum Oxide (AAO) template, exhibiting robustness of application with nanostructures. We finish with a brief overview of the contents of each chapter of this thesis.

Keywords: nanopore, nanocapillrray, DNA, protein, translocation, carbon nanotube, gas sensor, magnetoresistance, multilayered nanowire

1. Introduction

1. 1. Nanopore detection and analysis

Nanopore detection technique is a relatively new and versatile method that permits continuous single-molecule detection in solution without the need for labeling. This method, also known as nanopore sensing or resistive-pulse sensing, unites elements from four different scientific areas: biology, electrophysiology, electronics and nanotechnology. Single molecule analysis using nanopores allow important advanced in these fields.

The idea of biological nanopores inspired in lipid membranes as a tool since the analysis of single molecules was motivated by the very intense molecular transport activity between the intracellular and the extracellular media as well as between different cellular organelles. Molecular transport across the naturally-impermeable porous structures of cells occurs through a variety of protein channels incorporated

into the fluid mosaic of the lipid bilayers. These channels or pores act as gates through which a wide variety of molecules such as ions, nucleic acids, sugars and proteins can pass during their transport from one organelle to another, or from the cytoplasm to the outside of the cell. The ability of the pores to allow the passage of ions and larger molecules suggests that the ions can be used to flow an electric current. It could drive larger polar molecules through the channels. The change in the ionic flow through the channel due to the transfer of the macromolecule would depend on the structure of the particular translocating molecules.

Although biological pores have proved to be very useful study of biomolecular translocation, they have a number of disadvantages such as fixed size and limited stability. Typically the pores and lipid-bilayers can become unstable if external parameters such as pH, salt concentration, temperature, and mechanical stress, change. Solid-state nanopores present distinct advantages over their biological counterpart such as very high stability, control of diameter and channel length, adjustable surface properties and so on.

Similar to the natural molecular translocation mechanism through protein channels, the nanopore detection method utilizes a nanopore inserted into an insulating membrane separating two chambers filled with a buffer/electrolyte solution. The principle for nanopore detection is similar to the Coulter counter used for counting and sizing particles and is presented in Fig. 1. 1 [1]. An electric potential is applied across the membrane via two Ag/AgCl electrodes and the ionic current through the open pore is monitored with a patch-clamp amplifier. The patch-clamp amplifier is a very sensitive feedback amplifier able to maintain a

constant voltage while measuring low-level currents flowing between the two electrodes. When a charged molecule is driven into and through the nanopore by the electric potential, it causes a drop in the ionic current as electrolyte solution is displaced from the pore by the translocating molecules.
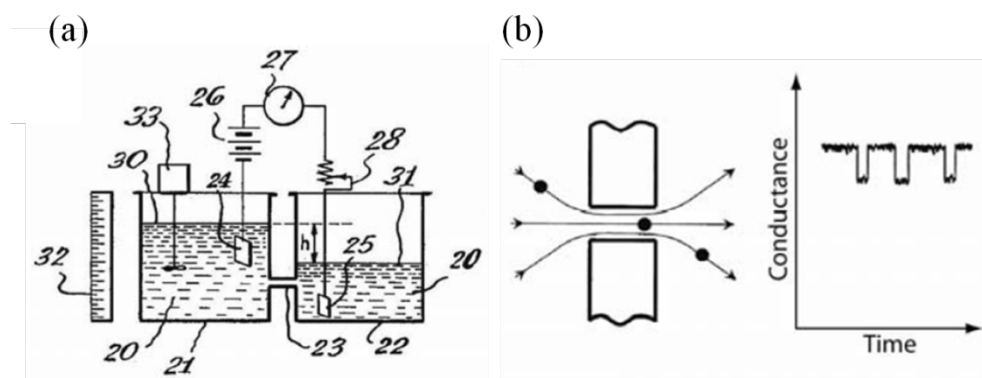
Fig. 1. 1 (a) Coulter counter patent. (b) Schematic of detection principle used in conventional coulter counters. As particles flow through a narrow constriction, they are detected as temporal conductance blockades.

The amplitudes (I_B) and durations (t_d) of the current blockade are measured by the patch-clamp amplifier, converted into digital data by a digitizer and finally sent to a computer for analysis. For a constant electrolyte concentration, pH value, temperature and applied potential the amplitudes are affected by the volume of the molecule while the duration times depend mainly on its length and charge. Furthermore, changes in the volume and length of the molecule are reflected in the two parameters mentioned above which are connected to the particular structure (typically molecule length and diameter) adopted in solution.

1. 2. Kinds of nanopores

Currently, there are two types of pores used for the nanopore detection method: protein pores and solid-state pores. The protein pores belong to the group of pore-forming toxins produced by bacteria with damaging effects on the cytoplasmic phospholipid bilayer of human and animal cells. Their innate property of auto-insertion into lipid bilayers played a crucial part in establishing this group of proteins as sensors.

Solid-state pores have been developed with the goal of improving the life span of the nanopore setup by using synthetic membranes, the range of molecules that can be analyzed by controlling the pore diameter as well as the range of experimental conditions that can be used (pH, temperature, ionic strength, applied potentials, etc.).

1. 2. 1. Protein nanopore

α-hemolysin from Staphylococcus aureus has been the most widely used pore since the inception of this method of analysis in 1996 [2]. This nanopore proved to have appropriate dimensions for single-molecule sensing as well as excellent stability, reproducibility and electric properties. The toxin is secreted as a 293 amino acid water-soluble monomer and has a molecular weight of 33.2 kDa [3]. The monomer binds to phospholipid bilayers and oligomerizes into a stable heptameric water-filled pore that subsequently auto-inserts into the structure of the bilayer [4]. When the toxin and phospholipid bilayers were assembled, the α-hemolysin pore adopts a mushroom shape approximately 100 Å in length and up to 100 Å in diameter with a hydrophilic interior and a hydrophobic exterior [5]. The extra-membrane cap domain forms a funnel-like vestibule with a maximum diameter of 46 Å and is connected with the stem domain through a 14 Å constriction (Fig 1. 2.). The trans-membrane stem domain is formed of 14 anti-parallel β-strands grouped in a right-handed β-barrel with a height of 52 Å and an intracellular end diameter of 20 Å. Being in direct contact with the membrane, the rim domain is involved in the stability of the pore within the lipid bilayer [5, 6]. Channel formation by α-hemolysin in reconstituted planar lipid bilayers was detected with patch-clamp instrumentation as discrete increasing steps in the membrane current, with each step corresponding to the insertion of a new pore [7]. The resultant current under an applied potential of 100 mV has a value of 100 pA for each channel inserted, conferring to α-hemolysin a conductance of 1 nS in 1 M

KCl at 22C [8]. The conductance, noise and ionic selectivity of the pore are sensitive to the pH and the electrolyte concentration with a minimum level of noise at pH values between 7.5 and 8.0 [9, 10]. Although the preference of α-hemolysin for anions, due to the charged amino acids surrounding inside walls, drops with increasing electrolyte concentrations, the pore maintains a slight anion-selective character even at high molar concentration of electrolyte (4 M KCl) [11, 12]. When α-hemolysin was inserted into the lipd bilayer, the channels maintain a stable open state for hours in concentrated KCl solution and only in the presence of mili-molar concentrations of divalent and trivalent cations undergoes a pH and voltage-dependent inactivation [7, 13, 14]. α-hemolysin has secondary and tertiary structural similarities with aerolysin, a toxin from Aeromonas hydrophila which has also been used in nanopore analysis.
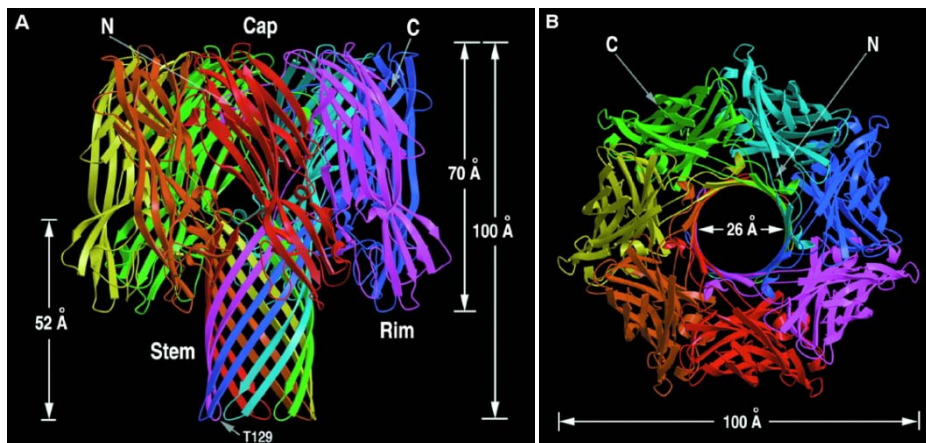
Fig. 1. 2. Ribbon diagram of the α-hemolysin pore showing the heptameric structure and dimensions. Image A shows the side view and image B shows the top view.

Aerolysin was identified in 1975 and later purified and sequenced by Bernhiemer, Howard and coworkers [15, 16]. Secreted as proaerolysin, a 470 amino acid inactive precursor with a molecular weight of 52 kDa, aerolysin becomes activated by proteolytic removal of a 25 amino acid C-terminal peptide [17, 18]. The activated aerolysin monomer concentrates at the membrane surface before it inserts as a heptameric aqueous pore complex [19, 20]. Although a crystal structure of the assembled aerolysin pore is not yet available, the electron microscopy image available shows that aerolysin is formed of a disk-shaped cap domain lacking the vestibule area present in α-hemolysin and a β-barrel transmembrane domain (Fig 1.3) [21]. The trans-membrane channel is approximately 80 Å in length and has an estimated diameter between 10 Å and 17 Å [21, 22]. Although the ability of aerolysin to form channels in planar lipid bilayers was reported for the first time in 1990, this nanopore was not used for nanopore detection until 2006 [23-25]. Discrete increasing steps in the trans-membrane current of 21 pA under an applied potential of 50 mV indicated a channel conductance of 0.42 nS for aerolysin [23]. Because aerolysin lacks the vestibule domain, its effective length is greater than that of α-hemolysin (10 nm). For ohmic behavior, the current through the nanopore is inversely proportional to its length, which explains the lower conductance of aerolysin compared to α-hemolysin despite a similar diameter. Furthermore, due to the lack of the bulky vestibule, aerolysin proved more resistant to urea denaturation than α-hemolysin and also presented a lower geometric and current asymmetry [26, 27].
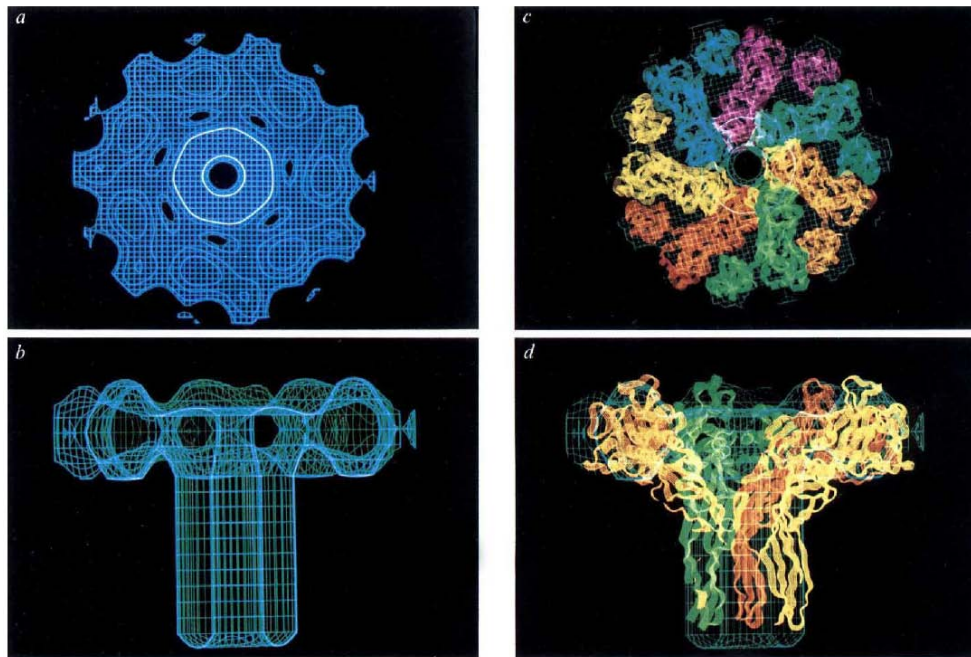
Fig. 1. 3. (a) Image of the aerolysin channel derived from electron microscopy when viewed down onto the membrane surface. (b) Side view of the image derived from electron microscopy. Structure of the aerolysin channel derived from electron microscopy. A side view of the channel is presented in image (c) and a top view in image (d)

MspA represents the main hydrophilic pathway across the cell wall of *Mycobacterium smegmatis* [28]. The mature MspA porin results after the cleavage of a 27 amino acids signal peptide and contains 184 amino acids with a molecular mass of 19.4 kDa [29]. The crystal structure of the porin was solved in 2004 and revealed a homooctameric goblet-like conformation with a central channel containing a 5 Å long, 12 Å wide constriction towards the periplasmic end (Figure 1.4) [30]. The porin is 96 Å long and 88 Å wide at the extracellular end while the internal diameter varies from 48 Å at the extracellular end to 10 Å at the periplasmic constriction. The large diameter of MspA accounts for the channel's high conductance values of 4.9 nS in 1.0 M KCl solution at 20C because the conductance is proportional to the diameter of the channel for ohmic behavior. MspA readily inserts into lipid bilayers presenting high thermal and chemical stability while being a cation-selective porin [29, 31].

The protein pores have the advantage of self-assembly and excellent pore-to-pore reproducibility in terms of electrical properties. They are also easy to engineer and have appropriate diameters for the detection of small molecules such as nucleic acids, peptides and small proteins [2, 32, 33]. On the other hand, protein pores have significant limitations: being assembled in fragile lipid bilayers it is uncertain if they could be incorporated into portable sensing devices. They also have a limited life span, a fixed diameter and only a limited number of experimental conditions can be tested without damaging either the bilayers or the pores. To overcome these limitations, several groups have developed synthetic or solid-state nanopores.
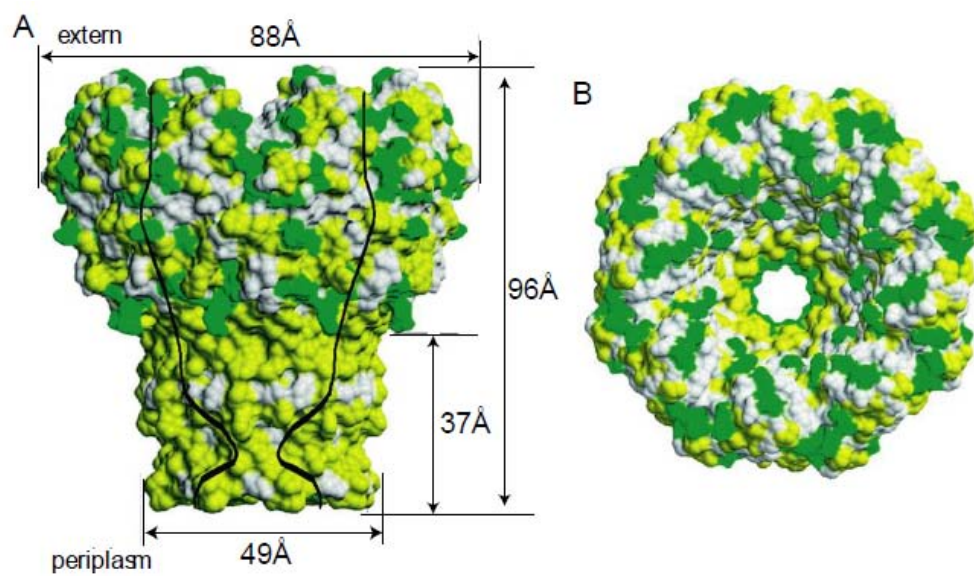
Fig. 1. 4. Structure and hydrophobicity map of the MspA porin. (a) side view of the channel is presented in image A and a top view in image (b).

1. 2. 2. Solid-state nanopore

During the past 10 years solid-state nanopore fabrication has seen major developments and currently such structures are starting to become commercially available. Depending on the material used, three main methodologies are commonly used for solid-state nanopore fabrication in insulating membranes: focused ion-beam drilling (in silicon nitride SiNx), focused electron-beam drilling (in SiO2, SiNx and graphene) and chemical track-etching (in polymeric films) (Fig. 1. 5).

The first solid-state nanopore used in single-molecule detection was generated in SiNx membranes using the ion-beam drilling technique [34]. At the beginning of the process, this method uses a focused ion beam (Ar^+) with energies of several thousand electron-volts (KeV) which removes layers of the material via sputtering (atomic scale erosion process) until it connects with a conical cavity preformed on the opposite side yielding a large pore (50 nm-100 nm) (Fig. 1. 5(a)). A diffuse ion beam is used during the second step of the procedure to narrow the pore down to the required diameter with a precision of ~1 nm via matter transport due to surface diffusion, viscous flow and redeposition [35, 36].

The control over the pore formation is maintained through a feedback system using an ion detector situated below the membrane which triggers the deactivation of the ion beam when the desired pore size is reached (Fig. 1. 5(a)). The pores fabricated with this method were asymmetrical in terms of geometry and electrical properties exhibiting a high preference for the transport of cations. This current

rectification was successfully corrected and thus the pores were rendered non-rectifying by an atomic layer deposition of an Al_2O_3 film [37]. Besides SiNx, other materials such as silica, SiO2, Cr, Al, poly(methyl methacrylate) and polyimide could be milled and shrunk in a similar way [38].

A different approach was tested by Cees Dekker's group at the Delft University of Technology which initially used electron beam lithography from a transmission electron microscope (TEM) and KOH etching to drill a larger pore (20 nm) in SiO2 membrane which was successively shrunk to the desired diameter by a diffuse electron beam following thermal oxidation (Fig 1. 5(b)) [39]. A major advantage of this technique is that direct visual feedback is possible through the TEM which allows controlling the pore diameter with single nanometer precision. A variation of this method uses a highly focused electron beam which can drill holes in free-standing SiO_2 membranes without the need of electron beam lithography. The diameter of the hole is fine-tuned with a diffuse electron beam as described above. Several groups have adopted the direct drilling approach to create pores (3 nm-30 nm) in SiNx membranes with accuracies of 0.5 nm, while others have designed nanopore arrays for parallelized single molecule detection (Fig 1. 5(b)) [40-42]. More importantly, here the shrinking process mechanism is different than the one reported for the ion beam drilling method. The electron beam appears to melt the SiO2 and SiNx membranes and due to the local surface tension the resultant pore adopts a symmetrical double cone structure which confers a non-rectifying electrical behavior to these pores (Fig 1. 5(b)). The solid-state nanopores used in the last part of the results section of this thesis were fabricated in SiNx using this

methodology [42]. Electron beam-drilled pores have also been fabricated in atomically-thin graphene membranes [43-45].

Ion-track etching is the oldest fabrication method for synthetic pores and has been used and improved since the 1960's [46]. The method uses heavy ions (Xe, Pb, Au or U) accelerated at very high kinetic energies (GeV) which allow the ions to penetrate layers of poly(ethyleneterephtalate) (PET), polycarbonate (PC) and polyimide (PI) leaving tracks into the material (Fig 1. 5(c)). These individual tracks are then isolated and chemically etched with a concentrated NaOH or NaOCl solution to generate pores down to 2 nm in diameter [47-49]. The etching process is stopped by neutralizing the basic solution with an acidic solution situated on the opposite side of the film immediately after penetration. The concentration and temperature of the etchant, as well as the duration of the process, are used to control the pore diameter, which is monitored either by scanning electron microscopy (SEM) or by conductivity measurements [49-51]. The pores resulting from this technique have conical shapes with transport properties dependent on the material and can be used for nanopore detection as well as ionic devices such as ionic diodes and ionic transistors [52, 53].

Although replacing the fragile lipid bilayer with a non-biological membrane improved the stability and the life span of the nanopore setup, other problems became apparent with these synthetic nanopores. One major problem arises from the relatively high capacitance of the SiNx material which is reflected in a much higher current noise and thus a lower signal-to-noise ratio than its biological counterpart [42]. More importantly, the analytes tend to adhere to the pore walls

and cause the pores to become permanently blocked, making single-molecule detection impossible. Another common problem with the solid-state nanopores is the poor pore-to-pore fabrication reproducibility with strong variations of the conductance and noise values between pores with the same nominal diameters[54].

Atomic layer deposition of alumina, polydimethylsiloxane curing on the SiNx membrane surrounding the nanopore, coating with organosilanes, polyethylene glycol (PEG) or complete lipid coatings of the pores are the main strategies used to improve the signal-to-noise ratio and to minimize the non-specific binding of molecules to the walls of the synthetic nanopores [37, 42, 55-57].
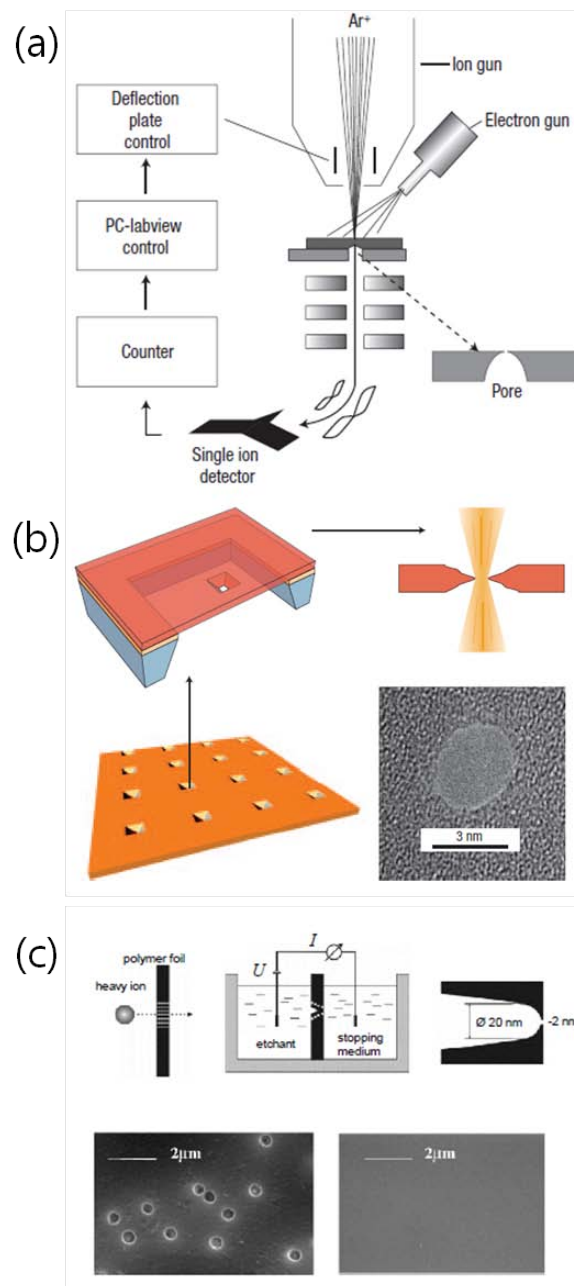
Fig. 1. 5. Fabrication methods for solid-state nanopores. (A) presents the ion-beam drilling method, (B) shows electron beam lithography and (C) illustrates the ion-track etching technique.

1. 3. Sensing with nanopores

Initially intended as a tool for DNA and RNA analysis with the long term goal of rapid nucleic acid sequencing, the method of sensing with nanopores was later extended for investigating a broad spectrum of molecules ranging from metal ions, small organic compunds and short peptides to chemical warfare agents, proteins and biomolecular complexes. In this section, the most significant advances in nucleic acid as well as in peptide and protein detection with nanopores will be presented.

The first report of single-molecule detection using nanopores was published in 1996 by Kasianowicz et al. and set the foundation of the nanopore sensing field. In their pioneering paper, the authors witnessed the translocation of individual single-stranded RNA and DNA molecules through the α-hemolysin pore as the ionic current through the pore was reduced by 85 % to 100 % [2]. The events histograms of poly[U] for instance, revealed three peaks with characteristic time values ranging from 0.095 ms to 1.288 ms under an applied potential of 120 mV. The duration of the faster events was found to be independent of the polymer length and the applied voltage and was thus ascribed to molecules colliding with the pore. The rest of the events had lifetimes proportional to their length and inversely proportional to the applied voltage indicating complete translocations through the pore. However, these events were grouped in two distinct peaks probably due to their different translocation orientation (3′ to 5′ vs. 5′ to 3′). The larger diameter of double-stranded DNA (~22 Å) did not allow for translocation, generating events

with similar characteristics to the colliding or bumping molecules mentioned above. In a separate experiment, addition of ribonuclease A (RNase A) to the cis chamber resulted in a sudden increase in the frequency of the current blockade as poly[U] molecules were sequentially cut by the enzyme into smaller segments. This result showed that the frequency of events was proportional to the analyte concentration and also proved possible the detection of enzymatic activity. The presence of single-stranded DNA molecules in the trans chamber was demonstrated by the polymerase chain reaction (PCR) [2].

More detailed studies of RNA and DNA translocation through α-hemolysin followed. Akeson and colleagues demonstrated that 130-150 nucleotide-long individual RNA molecules of poly[C], poly[A], poly[U] and poly[dC] can be distinguished from each other as the current blockade amplitudes and translocation times correlated to their individual secondary structures [8]. By examining the shapes of individual events of co-polymeric poly[A] and poly[C] molecules, a bi-level blockade was recorded corresponding to the translocation of the individual components. Besides being able to distinguish segments of different nucleotides within the same strand, these experiments also helped determine the orientation of the molecules during translocation. A preference for $3'$ to $5'$ translocation was found. The bi-level blockades disappeared upon digestion with RNase A which cleaves $3'$ pyrimidine residues. Furthermore, experiments conducted by Meller and coworkers distinguished between DNA molecules of similar length such as poly[dC]$_{100}$, poly[dA]$_{100}$, poly[dA$_{50}$dC$_{50}$], poly[dC$_{50}$dT$_{50}$] and poly[dAdC]$_{50}$ [58]. On one hand, the fact that sequence-specific information could be obtained from

the current signatures suggested that the nanopore method of analysis could be developed into a high-speed sequencing tool for RNA and DNA. On the other hand, due to the very fast translocation speeds (1-20 µs/nucleotide) compared to the rise time of the instrumentation (33 µs), it was concluded that to achieve single purine and pyrimidine nucleotide detection, increased resolution was needed [8].

One way to increase the time resolution was to lower the experimental temperature [58]. Experiments conducted at temperatures ranging from ˚15 C to 40˚C showed a pronounced decrease in translocation times at low temperature values. A translocation duration dependence on the temperature of $\sim T^{-2}$ was found for all DNA molecules tested. The separation of the peaks in the current blockade amplitude histograms proved to be best at low temperature values, suggesting that even lower temperatures would optimize the identification of individual polymers in mixed samples. Using this strategy, the authors were able to distinguish differences in sequences between same-length polymers down to 10 nucleotides [58].

Another way to increase the time resolution was to use single-stranded DNA molecules which formed hairpin structures with 2 to 10 base pairs stems [59-61]. In these experiments it was found that the hairpin molecules had to unzip to translocate the pore and that the transit time increased with the number of base pairs forming the stems of the hairpins. Further studies done on DNA hairpins demonstrated that the unzipping times decreased exponentially with the applied voltage [62]. The resolution was successfully improved while single nucleotide and

single base pair differences in the loop and/or the stem of the hairpin respectively could be detected with this strategy [59-61].

Furthermore, unzipping with nanopores proved useful for the detection of single point mutations in mismatched DNA duplexes [64]. A long biotinylated single-stranded DNA bound to streptavidin was not able to pass through the α-hemolysin pore but the single-stranded end can thread through to the trans side where it binds complementary DNA strands. The reversed applied potential value required for unzipping the double-stranded segment was inversely proportional to the number of mismatched bases present [64]. This ingenious experiment marked the starting point of the single-molecule force spectroscopy method. An offspring technique of nanopore sensing, this method studies the forces involved in the interactions between different biological molecules without the need for immobilization on solid supports as is required with molecular tweezers or atomic force microscopy [64].

It was also reported that chemically-tagged bases within a single-stranded DNA molecule slowed down the translocation and a characteristic current signal was obtained based on the modified/unmodified pattern. This approach allowed the discrimination between single nucleotide polymorphisms [65]. Recent results showed that single-stranded DNA translocation through α-hemolysin could be significantly decreased to about 4.1 ms for $(dA)_{20}$ by using electrolyte solutions containing organic salts and/or by introducing positive charges inside the lumen of the pore by site-directed mutagenesis [66, 67].

Other important results include the fact that the blockade frequency was proportional to the polymer concentration and that it increased exponentially with the applied potential. Single-stranded DNA molecules showed a higher propensity for translocation from the vestibule side of the α-hemolysin pore than from the stem side and their translocation in the 3′ to 5′ direction caused larger current blockades with faster durations than the 5′ to 3′ direction [62, 68, 69].

Despite the richness of knowledge about DNA translocation behavior through α-hemolysin, a DNA sequencing device based on nanopore sensing would not be possible without significant improvements in time sensitivity. The major obstacle in detecting individual nucleotides with α-hemolysin is the 5 nm long beta barrel domain which accommodates between 10-15 nucleotides at a given time which collectively affect the ionic current [70-72]. Since the residence time of each nucleotide inside this region is between 1-20 µs, it leaves only about 100 ions to mark the difference between two consecutive bases (a current of 2 pA). This cannot be resolved from the open pore noise unless the bases enter the pore separately or the thickness of the beta-barrel is similar to the thickness of one nucleobase [71].

Recent studies revealed that such a tool requires a much more complex setup. By using protein engineering, an α-hemolysin mutant pore (M113R) was created [73]. The mutant was designed to have high affinity for heptakis-(6-deoxy-6-amino)-β-cyclodextrin which was inserted through the stem end of the α-hemolysin pore and served as a molecular adapter with a smaller diameter for the sensing of 2′-deoxyribonucleoside 5′-monophosphates. The interaction between the nucleobases and the adaptor generated distinct current blockade values for each of the four

nucleobases so that they could be identified with 93-98% accuracy [73]. The blockade durations were very similar and could not be used for individual base identification. The method was further improved by covalently attaching the molecular adapter to the inside of the β-barrel which enabled the continuous identification of nucleoside ′5 -monophosphate molecules with 99.8% accuracy. The experimental conditions were adjusted to permit the activity of an exonuclease which sequentially digested single stranded DNA molecules while the individual bases were successfully identified by the pore-adapter complex [74]. This experiment suggested that the nanopore-based DNA sequencing tool will include an exonuclease genetically fused to the α-hemolysin pore in such a position that will allow the sequential capture of each cut nucleotide by the pore vestibule followed by translocation through the molecular adapter thus prohibiting the multiple detection of the same base. In another experiment, Cockroft et al. were able to identify each of the four nucleotides as they were added to an α-hemolysin-tethered DNA strand by an attached DNA polymerase [75]. Similar experiments were conducted with a variety of polymerases and were used to optimize the detection process [76-82]. In a different approach, Stoddart et al. succeeded in identifying three regions within the α-hemolysin pore capable of interacting with a DNA strand in a base-specific manner (recognition points). Using poly[dC] strands immobilized inside the α-hemolysin pore through a streptavidin-biotin complex fused to the strand and containing poly[dA]$_5$ blocks at different positions, the authors located the recognition points R1 (at the pore constriction), R2 and R3 within the β-barrel domain [83, 84]. Comparing the blockade current generated by

poly[dC] strands containing only one A base at different positions with that of poly[dC] of the same length, the single base difference could be recognized as long as the A base fell within one of the three recognition points. Furthermore, only R2 and R3 were able to distinguish between all four nucleobases during similar experiments [83, 84]. In the follow-up article, modified bases such as 5-methylcytosine and 5-hydroxy-methylcytosine could be distinguished in the same manner, which suggested that this approach could be used to identify epigenetic modifications in genomic DNA [85].

The single nucleotide sensitivity problem of α-hemolysin could also be overcome by using the channel protein MspA from Mycobacterium smegmatis. This octameric protein presents an ideal anatomy for single base identification with a single constriction of ~12 Å in diameter and ~5 Å in thickness [30]. By using a mutated version of MspA and slowing down the DNA strand translocation with double-stranded sections between each nucleotide of the strand to be sequenced, Derrington and coworkers were able to successfully identify each of the four deoxyribonucleotides [86].

Until 2001 only single-stranded and partially double-stranded nucleic acid molecules were tested in nanopore experiments. With the advent of the solid-state pores, double-stranded DNA molecules could be studied at last. While the detection principle remained the same, the effects of double-stranded DNA concentration, length and applied potential on the translocation signatures were systematically investigated with SiNx, SiO2 and polymeric nanopores of various diameters.

The first molecule to be detected with solid state nanopores was a 500 base pair (bp) double-stranded DNA which generated blockades of 12% of the ionic current through a 5 nm diameter SiNx pore [34]. Further experiments showed that SiNx pores could detect different levels of folding of double-stranded DNA molecules [87]. Comparing the event profiles, blockade amplitudes and durations obtained for translocations through a 3 nm pore with those through a 10 nm diameter pore, it was concluded that double-stranded DNA molecules with a diameter of 2.2 nm translocated the 3 nm pore in a linear conformation, whereas the much larger 10 nm pore allowed some of them to adopt a hairpin conformation during transit [34]. The linear DNA molecules generated classic one-step current blockade profiles, while the folded DNA molecules had two and even three-stepped profiles, depending on their conformation (Figure 1.6). Later it was found that using voltages higher than 200 mV decreased the number of hairpin conformations by linearizing the molecules [37]. Similar results were reported by several other groups who were also able to separately identify DNA strands of different lengths from a solution mixture [88-91], . Besides indicating the folding of double-stranded DNA molecules, larger synthetic nanopores were able to detect the translocation of paired molecules [34].

Furthermore, denaturation of DNA at high pH values was observed on an 8 nm diameter pore while at the same time double-stranded DNA and single-stranded DNA could be distinguished based on their translocation signatures [88]. The translocation velocity of double-stranded DNA molecules through SiNx pores proved to be two orders of magnitude faster than that of single-stranded DNA

through α-hemolysin, a very important set-back for the use of solid-state pores in DNA sequencing devices [37]. However, one order of magnitude improvement in time resolution was achieved by increasing the electrolyte viscosity (using 50 % glycerol), lowering the experimental temperature to 4 ˚C and decreasing the applied potential to 20 mV [92]. In contrast to the experiments performed with α-hemolysin, which showed a linear dependence between the translocation time and DNA length, solid-state pores confer a power law between the two parameters [89, 90]. The power exponent differs for shorter and longer DNA strands. This relationship was explained by the presence of a hydrodynamic drag that molecules transiting the larger solid-state pores experience with more pronounced effects on longer DNA molecules. Since the width of single-stranded DNA molecules is very similar to the diameter of α-hemolysin, hydrodynamic drag is not present when using biological pores. The blockade current varied linearly with the applied potential and the translocation times decreased with increasing applied voltage [89, 90] . Moreover, lowering the temperature and the pore diameter resulted in an increase of the translocation times of one order of magnitude [90]. Similarly to α-hemolysin experiments, SiNx pores with diameters less than 2 nm were used to forcibly unzip double-stranded DNA segments by driving them into the pore by an applied potential of 300 mV. The degree of complementarity between the two strands of the duplex DNA was reflected in the time required for the unzipping process, with slower times needed to unzip perfectly complementary duplexes and faster times when mismatches were present [93]. In a similar experiment, single-

stranded DNA hairpins needed less force to be unzipped in pores with diameters below 1.5 nm than in pores with larger diameters [94].

To date, solid state pores have proved useful for detection, sizing and determination of strand complementarity of DNA molecules but have been unable to distinguish between homopolymeric segments within individual strands or to identify single nucleotides. An ingenious advancement towards fast sequencing with solid state nanopores uses an extra pair of electrodes incorporated into the membrane structure in the vicinity of the nanopore. This approach promises to distinguish between individual nucleotides by tunneling currents through the bases and measuring their unique transverse current distributions with a scanning tunneling microscope or by perturbations in capacitance [96-100]. However, the fabrication of such nanopores is an extremely challenging task and so is the task of minimizing the noise and controlling the orientation of the bases inside the nanopore to allow proper contact with the embedded electrodes [96].

Recently, an optical recognition method has been proposed by McNally and colleagues. In this approach, the target DNA is first converted according to a binary code established by molecular beacons carrying two different fluorophores (yellow and red). When the beacons are stripped off by electrically driving the molecules through sub-2 nm diameter solid-state pores, photon bursts are detected by a total internal reflection imaging system. The color sequence generated reflects the sequence of the target DNA [101]. Although the method presents promise for high throughput parallelization, 23the steps required for sample preparation, labeling and code conversion represent a serious draw-back.

- 25 -

On one hand, there is the instability of the lipid bilayer in which the biological pores are inserted and on the other hand the challenge of solid-state nanopore fabrication with precise dimensions. These limitations may be overcome by integrating biological pores into solid state membranes resulting in hybrid nanopores as recently reported [102, 103]. Such a setup would provide a highly reproducible and indefinitely stable nanopore that will facilitate the process of DNA sequencing in the near future [72]. The newly-emerged graphene nanopores may represent a second approach to overcome the above-mentioned limitations. Being atomically-thin, these nanopores may prove advantageous for single-base identification either by ionic-current or tunneling current measurements [43, 44, 45].
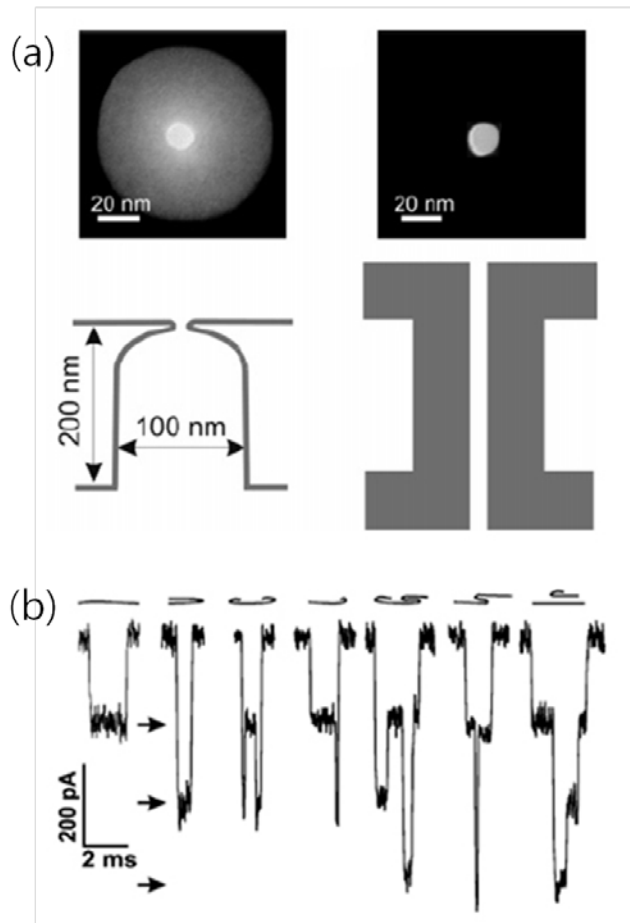
Fig. 1. 6. (a) Fabricated nanopores and nanochannels. TEM picture of an ion beam sculpted nanopore with 3 nm alumina ALD coating (top) and schematic of its cross section (bottom) (b) Seven translocation events (lambda-DNA through a nanopore) to further illustrate our observations and interpretations. The line diagram above each event indicates our interpretation. Arrows indicate the levels corresponding to blockades due to translocation of one, two, or three parallel lengths of DNA.

2. Solid-state nanopore for detecting of biomolecule

2. 1. Brief history

Detecting the change in electrical conductance or in resistance of a small pore in ionic solution containing particles has been used to count and size particles for decades. Wallace Coulter was attempting to standardize particle size in paints for the US Navy in the 1940s [1]. In order to solve this work, he invented a new measurement tool, based on a small aperture through which the particles would flow, restricting the flow of ions through the aperture as the particles passed. The story goes that one day he ran out of paint and instead tried a sample of his own blood. It was then that he realized that blood cells could be similarly detected. He patented his idea (Figure 1. 1), and later termed the 'resistive-pulse technique'.

For label-free sensing of single molecules, the availability of suitable nanopores is crucial. Although a number of methods exist to fabricate porous structures and

filter membranes obtaining a single hole in a thin membrane is a significant challenge.

There are two main sources for nanopores-biological protein pores, extracted, for example, from bacteria like *Escherichia coli* (e.g. outer membrane protein F) of *Staphylococcus aureus* (e.g. α-hemolysin), and fabricated ones derived from silicon nanotechnology. Despite the abundance of biological nanopores, it was a challenge to fine a nanopore that is stable for hours and has large enough ineer diameters to enable macromolecules like DNA to pass through them. To date, the most important sensing pore is without doubt α-hemolysin, which owing to its commercial availability is used for sensing in an ever-growing number of laboratories around the world [71].

One striking feature of biological nanopores is their atomic precision in assembly while providing almost perfect repeatability of nanopore structure. Anothoer main advantage of biological nanopores over man-made structures is the ability to use genetic modification to fine tune the nanopore properties [71]. This enables almost a free choice over their properties down to the single amino acid and even atomic level by mutagenesis. In effect, this was used in one of the earliest demonstrations of control of DNA in a nanopore whereby a single DNA strand in the pore was used to immobilize translocating DNA. A notable disadvantage, however, is most biological nanopores have diameters of less than 2 nm. This is suitable for sensing and sequencing of single-stranded DNA, RNA and unfolded protein chains but impedes the sensing of proteins in their native folded state or even double-stranded DNA. The search for larger diameter biological nanopores that possess tunable

diameters is ongoing.

Some of the shortcomings of biological nanopores have been addressed by the use of solid-state nanopores, with tunable diameters, first demonstrated by Li et al. [34]. Solid-state nanopores can be made in a variety of membrane materials by means of a focused electron or ion beams. The most common as carrier materials for the nanopores are silicon nitride membranes. Diameter, length and shape are only limited by the thickness and robustness of the membrane in salt solutions. For silicon nitride membranes, the thickness was reduced recently to a few nanometers, while with graphene nanopores, the nanopore length could be cut down to a single atomic layer. Recently, glass nanocapillaries were shown to be a relatively simple alternative approach for DNA sensing [104].

2. 2. Experimental details

Solid-state nanopore was fabriacated with the use of microfabrication technology to create free-standing membranes. The substrates are covered by a layer of 200 nm thin low stress silicon nitride (Si_3N_4) membranes, on both sides. Detailed fabrication is shown in Fig. 2. 2(a). Fig. 2. 2(b) show the optical image of silicon nitride membrane. We fabricate a single nanometer-sized pore through the use of a highly focused electron beam in a transmission electron microscope (TEM) or focused ion beam (FIB) technique in each membrane [34, 37]. Subsequently, the diameter of the fabricated nanopore can be enlarged with the highly focused beam or made smaller by exposure to a de-focused electron beam with lower intensity.

Due to the geometry of the reservoir cell and nanopore chip, there are several places air may be trapped during the filling of solution. The most troubling is the pyramidal pit etched in the silicon substrate, which can trap a bubble that is difficult to remove. To eliminate the problem of bubbles, all nanopore chips are treated in an oxygen plasma to make hydrophilic surface for about 30 s on both sides prior to use. If necessary, piranha treatment proceeds for 30 minute. Subsequently, the nanopores are mounted in a Teflon reservoir cell with PDMS gasket, and filled in salt solution two reservoirs. Reservoir cell covered with aluminum case to reduce electrical noise.

Ag/AgCl electrodes are used to detect ionic currents and apply electrical fields. Ag wire was cleaned in acetone, ethanol and DI water with ultrasonication in 10 min. Cleaned Ag wire dipped into chlorox solution about 30 min to form AgCl layer. An Axon Axopatch 200B (Axon Instruments, USA) patch clamp amplifier is used to make current measurement. (Fig. 2. 4(a)) The amplifier applies a constant voltage across the pore and measures the amount of current required to maintain the voltage drop. The measured current is low-pass filtered at 10 kHz (the bandwidth of the amplifier in resistive feedback mode is aroun 50 kHz) and digitized and continuously recorded at 100 to 250 kHz using Digidata 1440A (Molecular devices, USA). The power spectrum was recorded at 100 kHz using an internal Bessel filter at 10 kHz or 5 kHz bandwidth. Solution is exchanged in both reservoirs from 100 mM KCl to 1 M KCl (10 mM Tris, 1 mM EDTA, pH = 7.6) to perform DNA and DNA modified gold nanoparticles detection measurements.

For translocations measurements, λ-DNA (Bioneer inc.) and DNA modified gold

nanoparticle solution was added to the cis reservoir to a final concentration of 1 nM. The ionic current trace was recorded upon applying 120 mV, using a sampling rate of 100~250 kHz and an internal Bessel filter at 5 kHz or 10 kHz bandwidth. Current blockades occurring during translocations were recorded whenever a specific threshold was exceeded. Data analysis was performed in Clampfit and Origin 8.

(a)

Si₃N₄
Si (~500 μm)
Si₃N₄

Photoresist
Photolithography

Reactive ion etch

Anisotropic etch (KOH)

(b)

20 μm
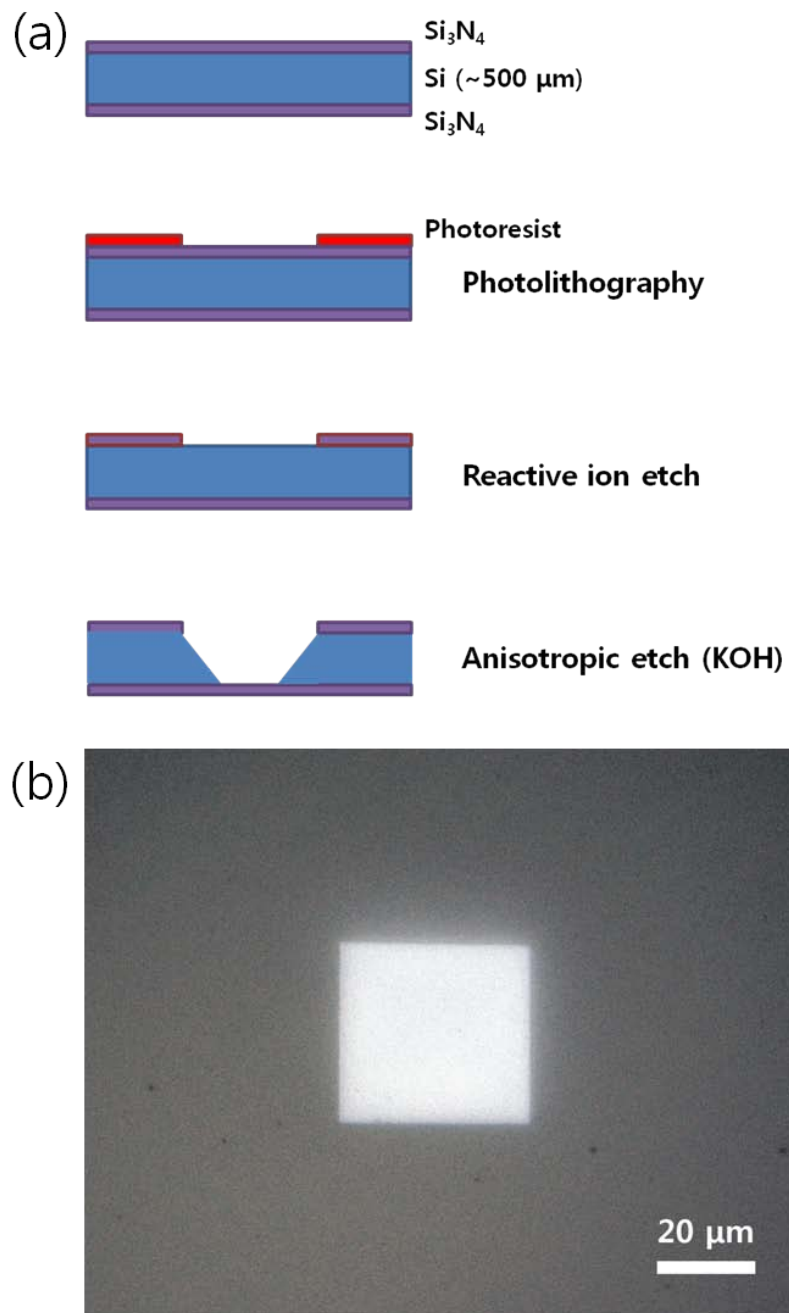
Fig. 2. 2. (a) Schematic diagram of silicon nitride membrane fabrication. (b) Optical image of silicon nitride membrane.
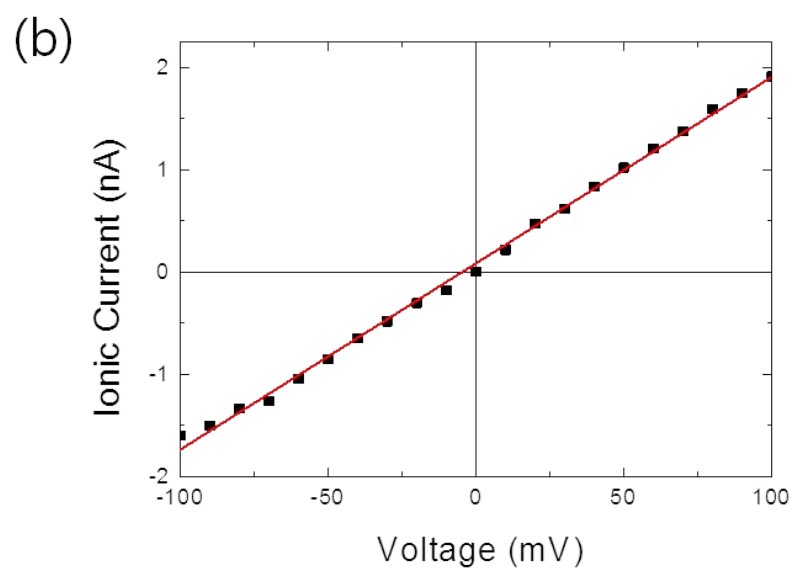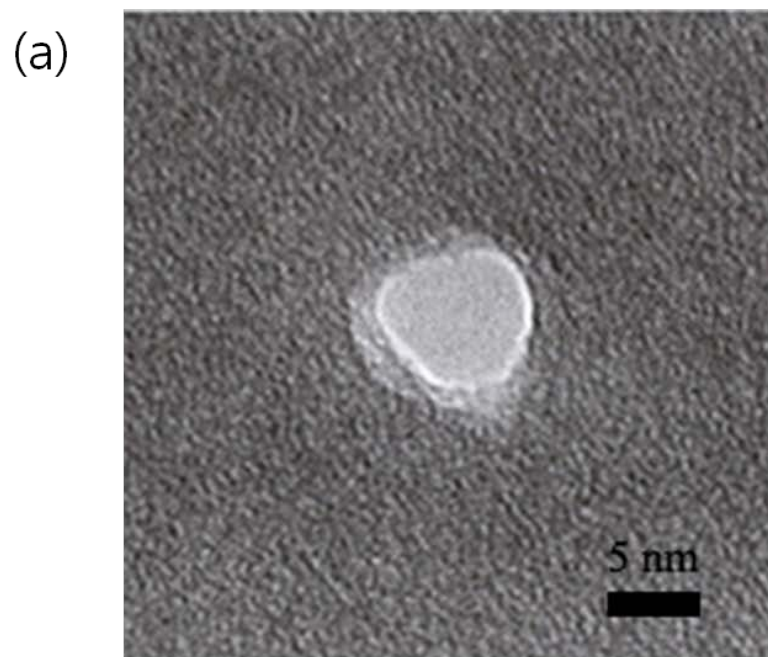
Fig. 2. 3. (a) TEM image of 10 nm nanopore. (b) Current versus Voltage curve for nanopore of 10 nm in diameter, where the solid lines are linear fits to the data.

Figure 2. 3(a) shows a TEM image of a fabricated solid-state nanopore of 10 nm diameter. In this study, we use nanopores with diameters from approximately 5 to 60 nm. TEM fabricated nanopore diameter is about 5 to 10 nm, and FIB fabricated nanopore diameter is about 50 to 60 nm. Figure 2. 3(b) is the plot of the current versus voltage curve in 1 M KCl solution with 10 nm nanopore. When voltage is swept from -100 mV to 100 mV, current characteristic are linear.

During translocation experiments, the baseline often shifts downward by an increment similar to the blockade induced by an translocation molecule. This shift, which is attributed to a molecule 'sticking' in the pore, can often be eliminated by reversing the driving voltage for a period of time.

All solutions were made using 18 MΩ deionized water. Generally, the most pure reagent grade was used. The buffer was generally maintained at pH 7.6 using 10 mM tris, and divalent ions were chelated using 1 mM EDTA and were purchased from Bioneer inc. The experiments are performed in a 1 M KCl in TE buffer. A schematic of the experimental lay-out in shown in Figure 2. 5.

(a)

(b)
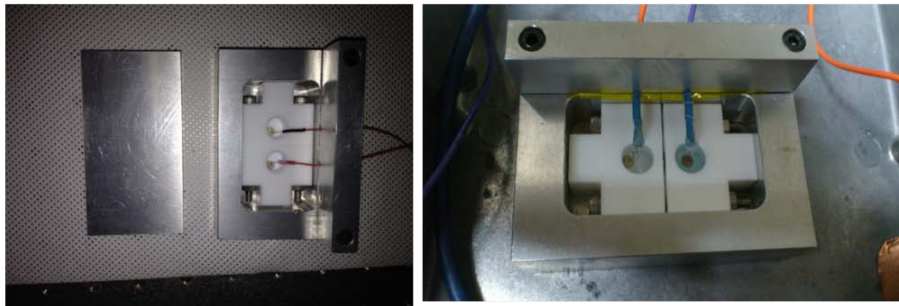
Fig. 2. 4. (a) Patch-clamp amplifier (Axopatch 200B, Axon Instruments). (b) Images of experimental setup. These are consist of Teflon cis and trans chamber with Aluminum box to reduce electrical noise.
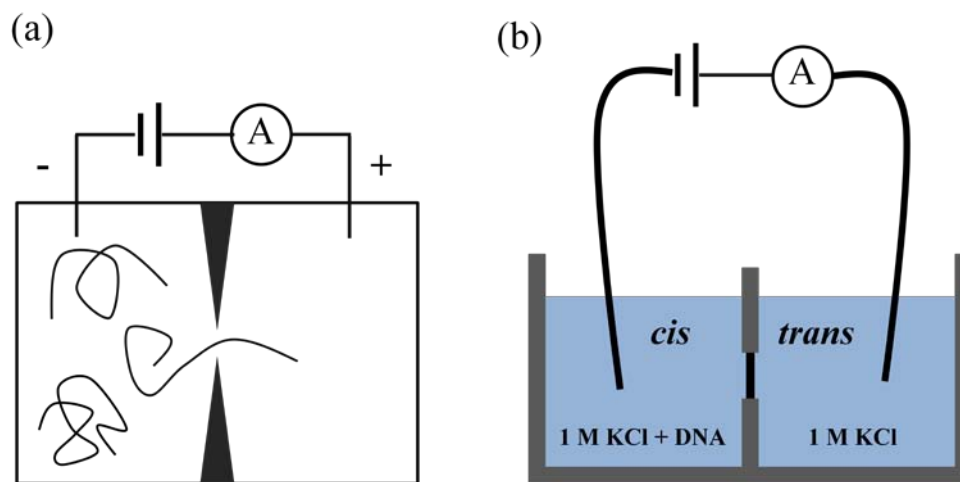
Fig. 2. 5. (a) Schematic layout of the experiment. A charged molecule is electrically driven through a nanometer-sized aperture, located between two reservoirs kept at a potential difference. The presence of a molecule inside the pore lowers the amount of conducting solution inside the pore. Passing molecules can thus be detected as short dips in the ionic current trough the pore. (b) Cross-sectional view of two reservoir system.

2. 3. Results and discussion

All nanopores are treated in an oxygen plasma for about 30 s on both sides prior to use. If needed, additional process was applied piranha treatment for 10 min. Subsequently, the nanopores are mounted in a Teflon cell, and sealed to liquid compartments on either side of the sample. Both compartments provide easy access for the placement of electrodes and exchange of solutions. Ag/AgCl electrodes are used to detect ionic currents and apply electrical fields.

This experiment has demonstrated that the translocation of a single molecule, which is recorded as a single translocation "event", often induces current blockades at quantized levels. To a first order approximation, the current blockage from the regions of the molecule that are translocating through the pore is equivalent to the total ionic current that can be carried by the volume of solution excluded from the pore by the translocating molecule,

$$I_b = \rho \times A \times V_{bias} / L_{pore}$$

where ρ is the solution conductivity, V_{bias} the applied voltage, L_{pore} the effective pore length, and A the hydrodynamic cross section of the translocating molecule [34, 37, 42]. Since the blockade current is linearly proportional to the hydrodynamic cross section of the translocating material, the translocation events exhibiting only one blockade level were interpreted as translocations of a single, double stranded DNA molecule that translocated through the pore in a linear, single-file manner.
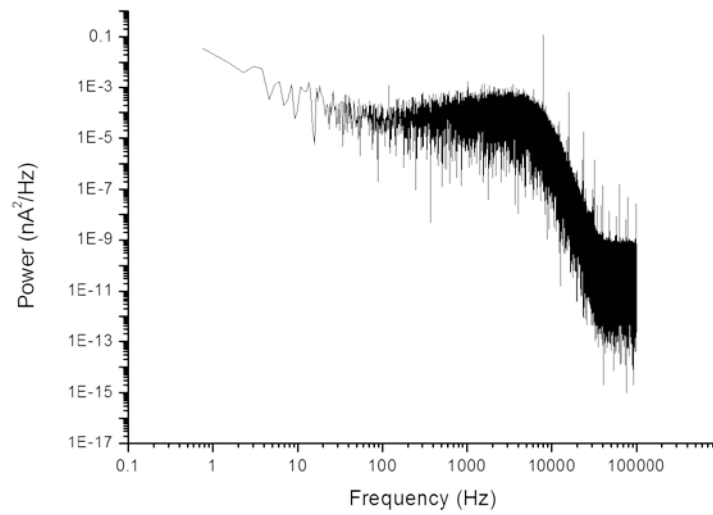
Fig. 2. 6. Power spectra of TEM fabricated nanopore with 10 nm diameter . Both measurements in buffered 1 M KCl, pH 7.6, at 120 mV.

We analyze the low-frequency 1/f noise in our solid-state nanopores. The nanopores analyzed have resistance values close to those expected from geometry. According to Hooge's phenomenological relation for low-frequency 1/f noise, the noise power, A, should scale inversely with the number of charge carriers Nc:

$$\frac{SI}{I^2} = \frac{A}{f} = \frac{\alpha}{N_c f}$$

where SI is the current power spectral density, I is the current, f is the frequency, and α denotes the Hooge parameter, which quantifies the amount of low-frequency noise [42]. Figure 2. 6 shows the current power spectral density $SI = I^2$ at low frequencies of a single nanopore. The trace shows 1/f type of noise behavior, with variation up to 2 orders of magnitude.

Figure 2. 7 shows current recordings of a 10 nm diameter nanopore at 120 mV after the addition of dsDNA molecules. When no molecules are present in solution, the ionic current recording displays a stable baseline with no significant deviations to lower or higher current values. Upon addition of λ-DNA molecules to the negatively biased compartment, short temporal current blockades appear. These blockades can be seen to reduce the ionic current through the nanopore to approximately 50~ 80 pA lower values. Figure 2. 8 shows enlarged current recordings of a 10 nm diameter nanopore at 120 mV after the addition of dsDNA molecules in a 4 cases. Fig. 2. 10 shows a histogram of 4 μs current samples. Note that each count in this histogram corresponds to a single current measurement, not to a single event. A typical recorded time trace lasts about 6 ms and therefore generates roughly 1000 counts in the histogram.

Fig. 2. 7. Current recording of a 10 nm diameter nanopore at 120 mV after the addition of λ-DNA to the negatively biased electrode.

Fig. 2. 8. Time-scale enlarged current recording of a 10 nm diameter nanopore at 120 mV after the addition of λ-DNA to the negatively biased electrode.

Fig. 2. 9. A histogram of 4 μs current samples of λ-DNA molecules.
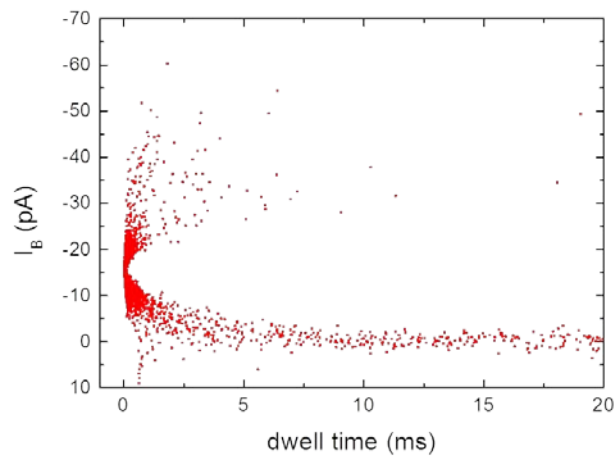
Fig. 2. 10. Scatter diagram of the amplitude of the conductance blockade versus translocation time for λ-DNA translocation through a 10 nm diameter nanopore Each point in this scatter diagram corresponds to a single translocation event. Applied voltage is 120 mV.

We now analyze the translocation events of λ-DNA molecules according to their conductance blockade and time duration. All events with conductance blockades that exceed the nanopore current noise are taken into account. The value of the conductance blockade is determined with respect to the open-pore conductance and represents the average blockade over the time duration of the event. The open-pore conductance is simply the average conductance and we define that events begin and end when the conductance deviates one standard deviation from this average. Figure 2. 10 shows current recordings of a 10 nm diameter nanopore at 120 mV after the addition of ladder DNA molecules. When no molecules are present in solution, the ionic current recording displays a stable baseline with no significant deviations to lower or higher current values. Upon addition of λ-DNA molecules to the negatively biased compartment, short temporal current blockades appear. These blockades can be seen to reduce the ionic current through the nanopore to approximately 60~ 70 pA lower values.
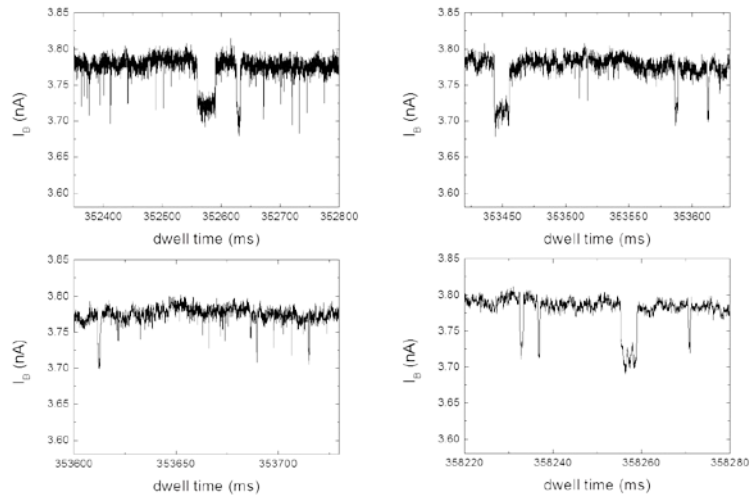
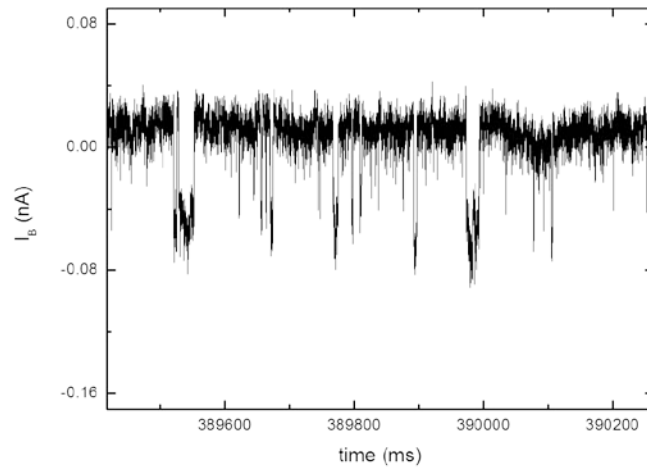Fig. 2. 11. Current recording of a 10 nm diameter nanopore at 120 mV after the addition of ladder DNA to the negatively biased electrode.

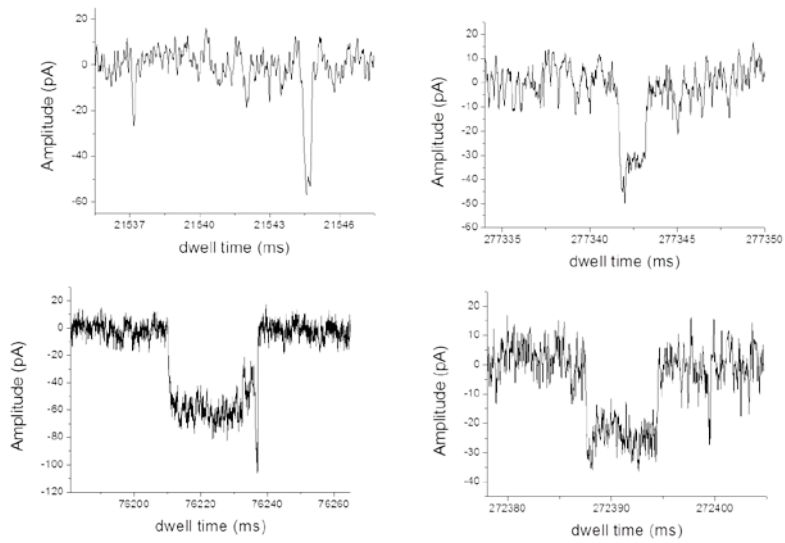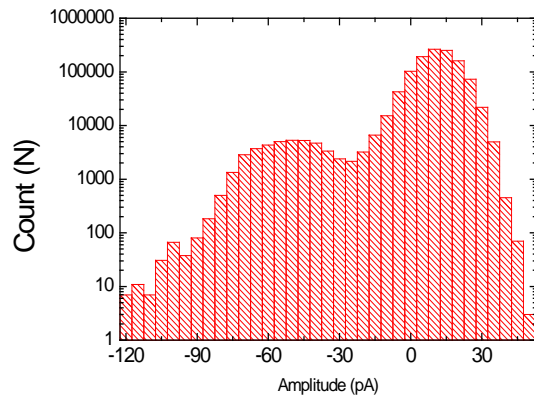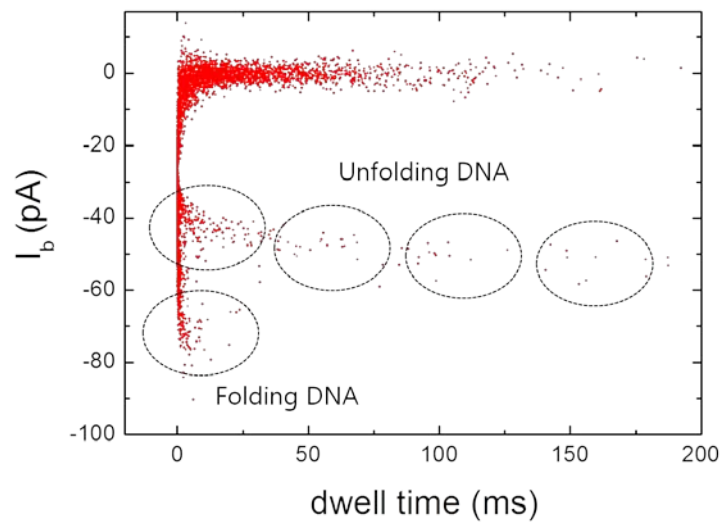Fig. 2. 12. Scatter diagram of the amplitude of the conductance blockade versus translocation time for ladder DNA translocation through a 10 nm diameter nanopore. Each point in this scatter diagram corresponds to a single translocation event. Applied voltage is 120 mV.

Figure 2. 11 shows the conductance blockade versus time duration of ladder DNA translocation events in a scatter plot. The measurements are performed using a 10 nm diameter nanopore and at a bias voltage of 120 mV. The events show a variation in both the current blockade and the event duration.

Further analysis of individual events was performed using a dedicated pClamp 10 program. For each recorded event, the open pore current was determined from the pre-trigger part of the measurement. During the experiment the open pore current slowly drifts due to small potential drifts caused by the Ag/AgCl electrodes and concentration changes due to evaporation.

Measurements of ionic currents through solid-state nanopores revealed that the electronic noise in many sample exeeded that from the source. A pore was deemed inadequate for use as a DNA translocation if its total peak-to-peak noise was within approximately one half the expected blockade amplitude for a nanopore tranlocation. The number of successful DNA detection experiments was limited by the observed excess noise. In most cases the peak-to-peak noise level would completely obscure any DNA signal. Many sample, however, exhibited acceptable noise characteristics for DNA detection.

2. 4. Summary

Solid-state nanopores can be used to measure the diameter, length and conformation of a translocating DNA molecule. There is hope that similar measurements may be made on translocating proteins, whos structure and

conformation are more interesting research questions, and that integrated electronics may allow direct interrogation of translocating molecule's chemical structures. All these measurements will be enhanced by repeated measurement of the same molecule in the configuration. The availibility of a single molecule detection based a solid state nanopore is thus the most important and broadly applicable result presented.

3. Nanocapillary for detecting of biomolecule

3. 1. Motivation

Nanopores offer an attractive platform for addressing a number of challenging questions in chemistry, biotechnology and materials science. One of the oldest and simplest routes to form a single nanopore is the nanopipette. Sensing is achieved through recognition of target DNA sequences hybridized to complementary probe sequences bound to the nanopipette surface. Upon recognition, the anionic charge at the surface of the nanopipette is increased, resulting in a change in the observed rectification of ionic current which flows through the nanopipette under an applied potential [71, 72].

Ion current rectification is a phenomenon observed in many protein channels, and is often inherently related to the selective transport of ions and

molecules. Synthetic nanopores that are asymmetric in shape and possess diameters comparable to the double layer thickness of electrolyte solution employed can also exhibit non-Ohmic, rectified current–voltage responses. Synthetic nanopores which rectify can be obtained *via* a number of routes, including track-etch ploymer films, solid-state nanopores, and pipettes. Siwy and co-workers have reported detailed investigations associated with the charge distribution, geometry, and resultant rectification properties for conical nanopores prepared in polymer films [47-50, 53]. For synthetic conical nanopore geometries, rectification is largely dependent on the cone angle of the pore and the charge present at the surface of the nanopore.

If an analyte binds to the surface of a nanopore, a change in the charge at the surface of the nanopore is often generated. Analyte binding can thus be transduced by changes in the extent or magnitude of rectification as a result of the change in surface charge after binding. This effect has been used to detect proteins, drug molecules and polymers using conically-shaped nanopore platforms. Nanopipettes offer a convenient route to nanopores with the often-beneficial material properties of silicate glasses. A simple route to glass nanopores of defined size and dimension is found through the use of automated pipette-pullers to prepare pulled-glass pipettes. Traditionally, pulled-glass pipettes are employed in electrophysiological settings, and are used to prepare patch-clamp electrodes or needles for microinjection. The ability to produce nanometre-scale openings at the tip of a pulled-pipette has been recognized for many years, but recent investigations of these high-resistance nanopipettes have expanded their use and application [104],.

3. 2. Experimental details

  Quartz and glass capillaries with an outer diameter of 1 mm and an inner diameter of 0.7 mm (Sutter instrument, USA) were used for all experiments. Prior to pulling the capillaries, the glass pipettes were thoroughly cleaned by sonicating in acetone and ethanol for a duration of 5 min in each step. This removed any contamination resulting from the production process or dirt acquired during transport, storage, and handling. Residual ethanol from the cleaning process was removed with gaseous nitrogen. Afterward, the capillary ends were attached to the pulling slides in the pipet laser puller. The CO_2 laser heated a spot of 0.1 mm in the middle of the capillary. Meanwhile the glass capillary was pulled in opposite directions at both ends. Consequently, the glass shrank in diameter in the heated area. A final stronger pull separated the capillary in the middle resulting in capillary tips of identical shape and with the same diameter. Fig. 3. 1 shows nanocapillaries with inner diameters as small as 50 nm as shown in the scanning electron microscopy (SEM) images. Prior to visualization in the SEM, nanocapillaries were coated with a 10 nm thick layer of platinum (Pt).
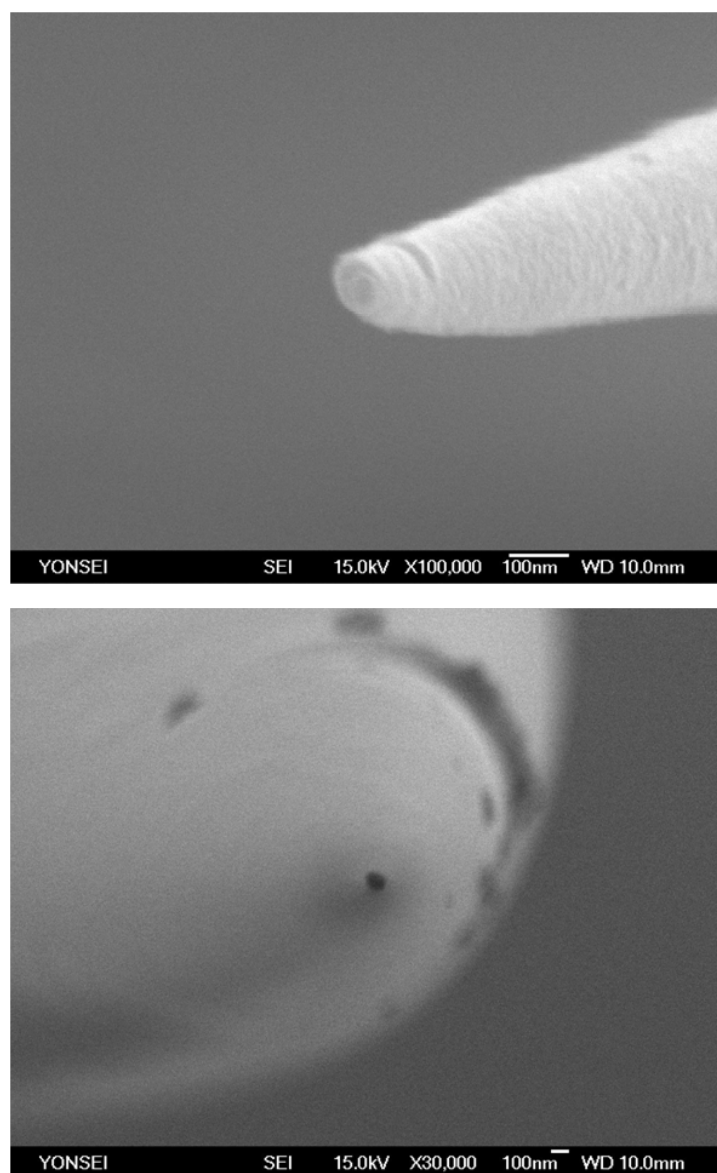
Fig. 3. 1. SEM images of glass (Top) and quartz (bottom) nanocapillay after pulling with a laser-assisted pippet puller. The nanocapillay was coated with a 10 nm thick Pt layers to prevent charging effect.

For translocation experiments nanocapillaries were mounted into a PDMS cell, connecting two reservoirs (see Figure 3. 2(b)). In each chamber a 200 μm diameter silver electrode was embedded which was chlorinated (Ag/AgCl) in chlorox solution for 30 min before the measurement. One electrode was mounted into the reservoir in front of the nanocapillary tip. The other electrode was passed through the glass capillary until it touched the conical part of the capillary (see Figure 3. 2(b)). Afterward, the two reservoirs and the micropipette were filled with potassium chloride (KCl) solution of 500 mM. We kept the pH at 7.6 throughout all experiments by using 10 mM Tris and 1 mM EDTA solution. Air was completely removed from the flow cells and nanocapillaries by placing the assembled cells into desiccators and evacuating with a vacuum pump for around 30 min. Before the experiment started, the electrode offset was set to zero, and the nanocapillary was tested for stable current-voltage characteristics and a root mean square (rms) of the ionic current signal below 10 pA. During the experiment, the ionic current was checked regularly for stable current-voltage characteristics. The λ-DNA (Bionner, Korea) and bovine serum albumin (BSA) was diluted by 1:10 to a 10 nmol/L concentration and added to the reservoir as close as possible to the tip of the nanocapillary. For all ionic current measurements we used the Axopatch 200B (Axon Instruments, USA) amplifier in voltage-clamp mode with the internal four-pole Bessel filter at 10 kHz bandwidth. The signals were digitized with a Digidata 1440A (Molecular devices, USA). Data recording was performed with a pClamp 10 program (Molecular devices, USA). Voltage-driven translocation of λ-DNA showed a characteristic decrease in the ionic current which was recorded whenever

a specific threshold was exceeded. For statistical analysis, between 400 and 1000 translocation events were recorded.

The solution (1 M KCl, 10 mM Tris, 1 mM EDTA, pH = 7.6) was filtered (0.22 μm Millipore syringe filters), heated at 70 ºC and added to the two reservoirs immediately after the plasma cleaning process. Finally, the assembled cell was placed under vacuum in a desiccator to remove air bubbles in the capillary for approximately 1 min. Silver electrodes (200 μm diameter) were chlorinated (Ag/AgCl) and inserted in both reservoirs. The electrode in the *cis* reservoir was connected to ground and the one in the *trans* reservoir was connected with the amplifier headstage. An schematic representation of the nanocapillary cell is shown in Fig. 3. 2(a).

The recorded data analysis was done with the Clampfit software contained within the pClamp 10 packages from Axon Instruments. There are three main types of windows in Clampfit: analysis, results and layout. Recorded data was opened in the analysis window, displayed as a series of concatenated episodes of events and visualized in the browse mode so that the important features of the signals could be observed.

This type of interaction can generate large I values similar to translocations but their T values in fact increase with increasing applied voltages. In this situation, the molecules enter the nanopore temporarily and then diffuse back out exiting on the same side they entered. Translocations and intercalations can only be distinguished through nanopore sensing experiments carried out under a range of increasing applied voltages while monitoring the blockade ion variation.
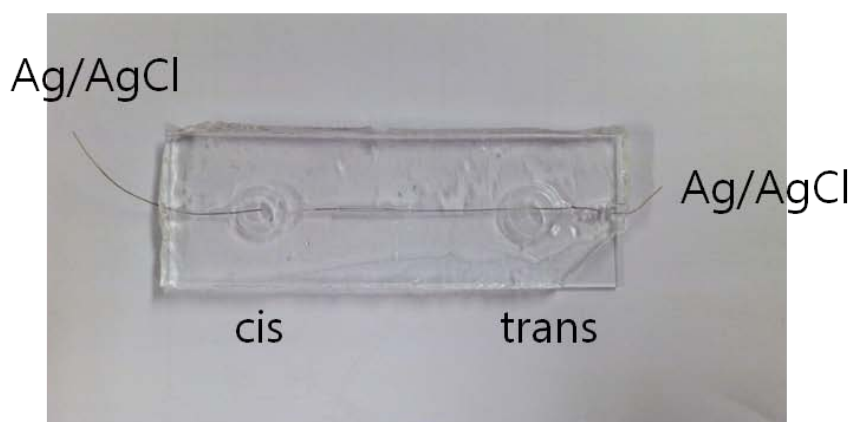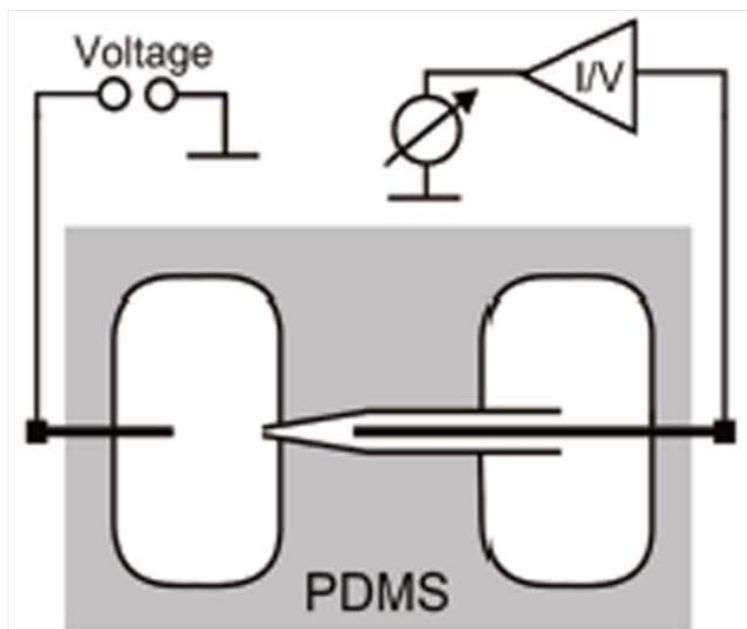
Fig. 3. 2. (a) Schematic of experiment (b) Optical image of PDMS cell with nanocapillary and Ag/AgCl electrode.

Once a zone of interest on the displayed data was identified, the next step was to select this segment for the Clampfit analysis. For the event detection step, one or two detection thresholds were used. On one hand, if the acquired data was formed of only one type of event, then a single detection threshold was sufficient. On the other hand, if two distinctive populations of events belonging to two different blockade amplitudes and times were identified, using two detection thresholds enhanced the separation and ease of analysis. After the segment to be analyzed was selected and the thresholds placed, the program scanned through the data approximating the amplitude and calculating the duration of each event crossing the thresholds using a non-stop level detection mode. In our protein pore experiments, any event with current blockade amplitude at least three times larger than the membrane noise was recorded. Once the event detection session for 79 the selected segment was complete, the features of each event could be observed in the event viewer window. There it was much easier to notice the presence of one or more populations of events belonging to different blockade amplitudes and durations or identifying and rejecting unwanted signals from the analyzed data.

Furthermore, Colquhoun and Sigworth suggest that the amplitude of a channel blockade can be measured accurately only if the event duration is twice the rise time of the recording system. In our experiments we considered any transition 50 µs or less to be too fast to be correctly measured and the events were not included in our calculations.

Resolution of the amplitude is determined by the filter frequency and the sampling rate. Clampfit calculates the amplitude by averaging the data points in the

level after dropping the first and last points to eliminate interference from filter attenuation (PClamp).

After the analysis was finished, the individual characteristics of each event were found in the results window as a spreadsheet of all durations and amplitudes listed in sequence by their start time in the original file. Further on, we examined the results spreadsheet in Clampfit and imported it into Origin graphing software (OriginLab Corporation). The imported data was organized in histograms of current blockade amplitudes and blockade durations versus the number of events. The amplitude of the blockade current populations was determined by fitting each blockade current distribution with the Gaussian function. The lifetime data was obtained by fitting each blockade duration distribution with a single exponential decay function. Curve fitting was done using Lavenberg-Marquardt method. The standard deviation of the function was used to evaluate the goodness of the fit.

3. 3. Results and discussion

All nanocapillaries are treated in an oxygen plasma for about 30 s prior to use. Subsequently, the nanocapillaries are mounted in a PMMA cell or PDMS cell, and sealed to liquid compartments on either side of the sample. Both compartments provide easy access for the placement of electrodes and exchange of solutions. Ag/AgCl electrodes are used to detect ionic currents and apply electrical fields. Figure 3. 3 is the plot of the current versus voltage curve in 1 M KCl solution with 50 nm nanocapillary. When voltage is swept from -100 mV to 100 mV, current

characteristic are linear. All solutions were made using 18 MΩ deionized water. Generally, the most pure reagent grade was used. The buffer was generally maintained at pH 7.6 using 10 mM Tris, and divalent ions were chelated using 1 mM EDTA and were purchased from Bioneer inc. The experiments are performed in a 1 M KCl in TE buffer. Figure 3. 4 shows the current power spectral density $SI=I^2$ at low frequencies of a single nanopore and single nanocapillary. The power spectral density of nanocapillary was lower than the nanopore.

  Figure 3. 5 shows current recordings of a 50 nm diameter nanocapillary at 120 mV after the addition of BSA molecules. When no molecules are present in solution, the ionic current recording displays a stable baseline with no significant deviations to lower or higher current values. Upon addition of BSA molecules to the negatively biased compartment, short temporal current blockades appear. These blockades can be seen to reduce the ionic current through the nanopore to approximately 60~ 120 pA lower values. Figure 3. 6 shows enlarged current recordings of a 50 nm diameter nanocapillary at 120 mV after the addition of BSA molecules in a 4 cases.
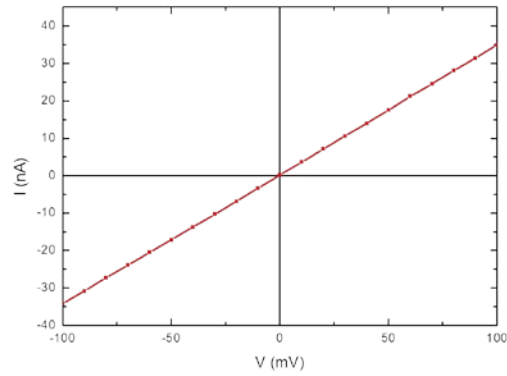
Fig. 3. 3. Current versus Voltage curve for nanocapillary of 50 nm in diameter, where the solid lines are linear fits to the data.
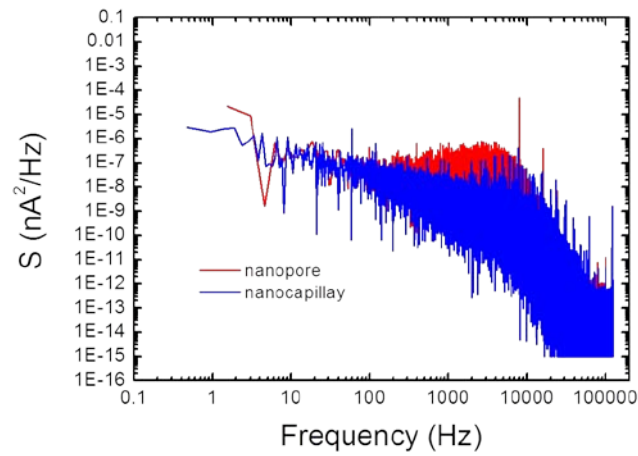
Fig. 3. 4. Power spectra of nanopore and nanocapillary. Both measurements in buffered 1 M KCl, pH 7.6, at 120 mV.

Fig. 3. 7 shows the current trace histogram for BSA translocations (logarithmic scale) when applying 120 mV in a nanocapillary studied at 500 mM KCl (pH=7.6). For each event the mean baseline current is subtracted before generating the histogram. Note that each count in this histogram corresponds to a single current measurement, not to a single event. A typical recorded time trace lasts about 6 ms and therefore generates roughly 2000 counts in the histogram.

Figure 3. 8 shows current recordings of a 50 nm diameter nanocapillary at 120 mV after the addition of DNA modified Au nanoparticles. Upon addition of BSA molecules to the negatively biased compartment, short temporal current blockades appear. These blockades can be seen to reduce the ionic current through the nanopore to approximately 200~ 400 pA lower values.
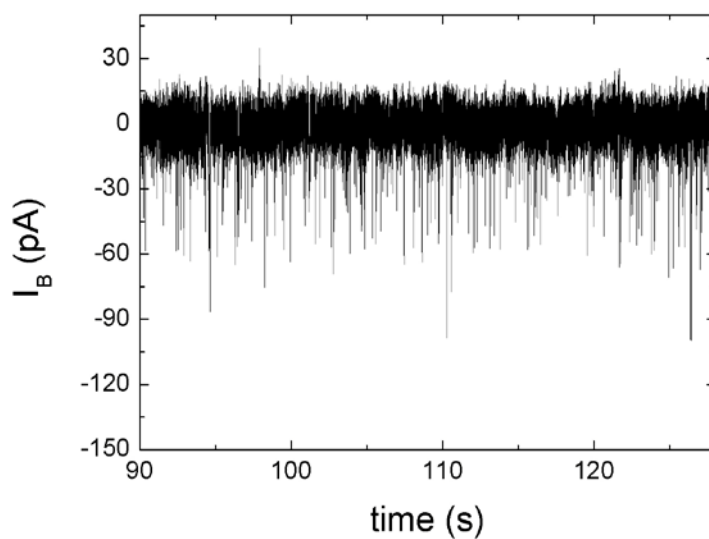
Fig. 3. 5. Current recording of a 50 nm diameter nanocapillary at 120 mV after the addition of BSA to the negatively biased electrode.
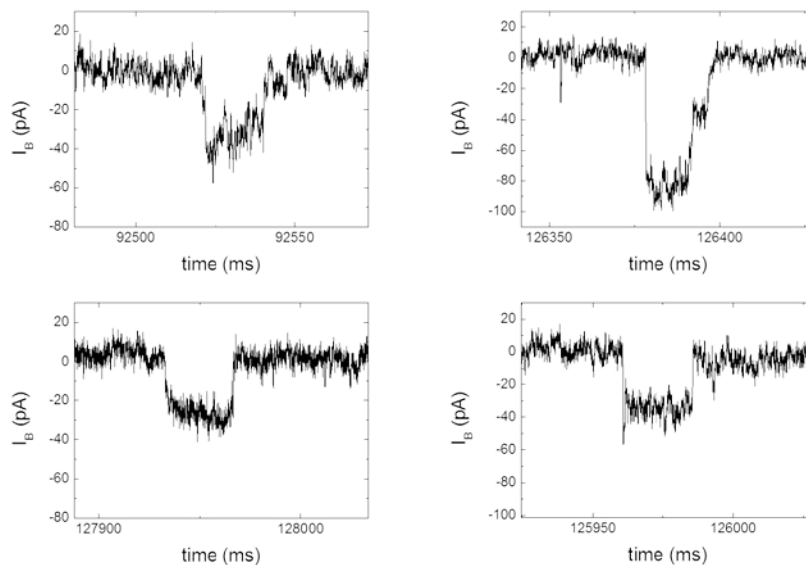
Fig. 3. 6. Current recording of a 50 nm diameter nanocapillary at 120 mV after the addition of BSA to the negatively biased electrode.
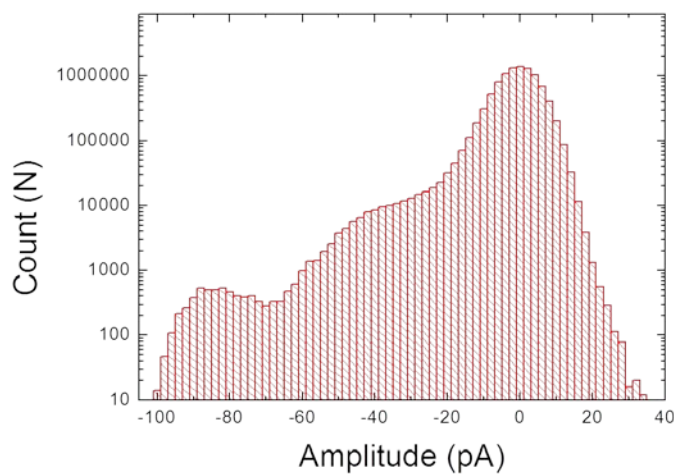
Fig. 3. 7. The current trace histogram for BSA translocations (logarithmic scale) when applying 500 mV in a nanocapillary studied at 500 mM KCl (pH=7.6). For each event the mean baseline current is subtracted before generating the histogram.
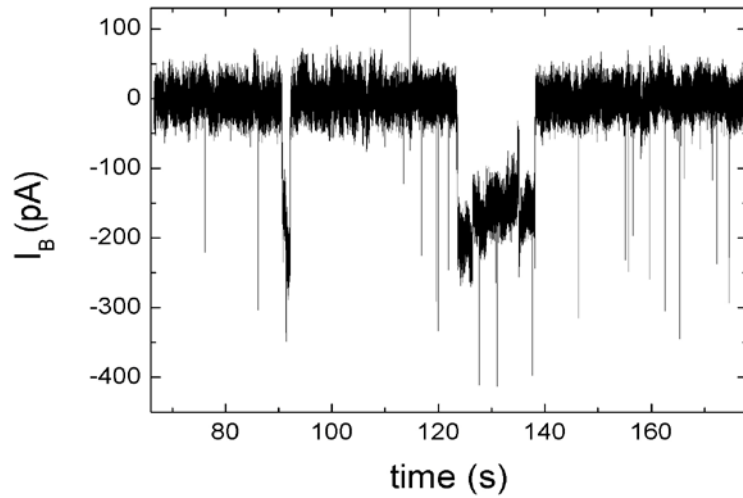
Fig. 3. 8. Current recording of a 50 nm diameter nanocapillary at 120 mV after the addition of 10 nm DNA modified Au nanoparticles to the negatively biased electrode.

3. 4. Summary

We have been discussing a nanocapillary based sensor for the detection of BSA and DNA modified Au nanoparticles. Our setup can detect a single BSA molecule and DNA modified Au nanoparticle. For the latter finding we investigated the current histogram of the events which revealed the existence of several current levels. Our results demonstrated the possibility of nanocapillaries as a promising alternative to solid-state nanopores for label-free single molecule analysis.

4. Electrically refreshable carbon-nanotube-based gas sensors

4. 1. Introduction

Carbon nanotubes as chemical sensors have received considerable attention because of their high surface-to-volume ratio, radii comparable to the Debye length, and unique electrical properties [106-112]. Upon exposure to gas molecules, the electrical conductance of CNT changes and the threshold voltage is shifted due to charge transfer between the semiconducting CNT and the electron donating/withdrawing molecules. CNT chemical sensors offer significant advantages over conventional metal-oxide-based electrical sensors in terms of sensitivity and room temperature operation. Nevertheless, there are several problems to overcome for their practical application. First, it takes a long time for the CNT chemical sensor to refresh at room temperature, since an activation energy

for desorption is usually higher than the thermal energy. UV illumination [108] and heating [109] have been used to shorten the recovery time, however it is not convenient to integrate a UV source or a heater with a sensor. Second, CNT chemical sensor lack selectivity. The electrical conductance of CNT decreases in several gases such as NH_3, ethanol, benzene, etc. and increases in NO_2. Therefore, it is difficult to distinguish the adsorbed species by just measuring the conductance change. Polymer functionalizations were shown to impart selectivity to the CNT sensor [110, 111], but they are very limited. Here, we report an electrically refreshable CNT based chemical sensor. A back-gate voltage has been used to refresh the sensor. In addition, the temporal response of the conductance to the gate voltage pulse demonstrates the feasibility of distinguishing adsorbed molecules.

4. 2. Experimental details

The CNT gas sensor was fabricated base on a field effect transistor (FET) structure as shown in fig. 4. 1. The single-wall carbon nanotubes (SWNTs) were grown by the patterned catalyst growth technique [113]. Co catalysts were patterned on heavily doped Si substrates with a 300 nm thick thermally grown SiO_2 layer. Then, SWNTs were grown by chemical vapor deposition (CVD) using a mixture of methane and argon as the carbon source at 900 ^{o}C. The growth was maintained about 10 min. Source (S) and drain (D) electrodes were made by depositing Cr/Au (5 nm /50 nm) and using a lift-off technique, followed by rapid thermal annealing at 500 ^{o}C for 60 s in nitrogen

atmosphere to form good contacts. Fig. 21 shows schematically whole process about CNT gas sensors fabrication. To determine whether the CNT connected between source and drain electrodes was metallic or semiconducting, the source/drain current (I_{SD}) was measured as a function of the bottom gate voltage (V_{BG}) for all devices. The heavily doped Si substrate was used as the bottom gate and electrical measurements were carried out using a semiconductor parameter analyzer (Keithley 4200-SCS). An atomic force microscope topography of the device is presented in Fig. 22(b); the CNT has a length $L \approx 1$ μm and a diameter $d \approx 1$ nm as determined from the height profile of this image. For chemical sensing experiments, the CNT sensor was mounted into a small chamber with electrical feedthrough. This chamber was pumped down to 10^{-3} Torr and filled with the target gas diluted in argon.
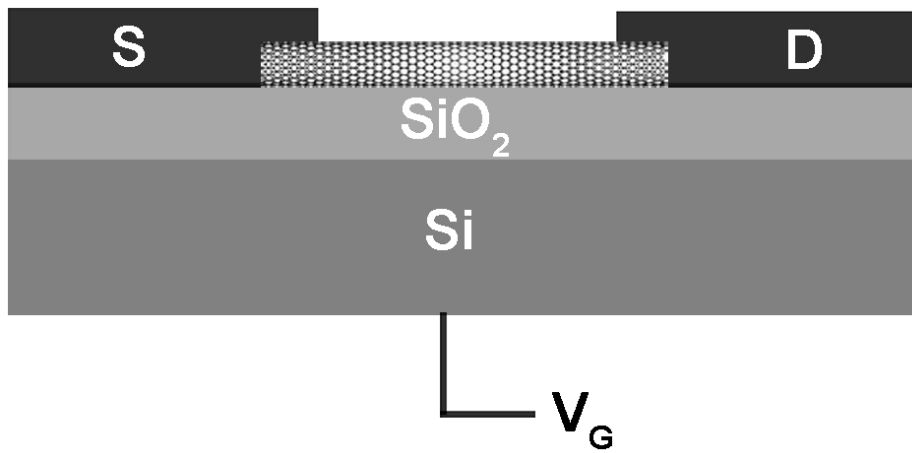
Figure 4. 1. Schematic diagram of the carbon nanotube-field effect transistor (CNT-FET).
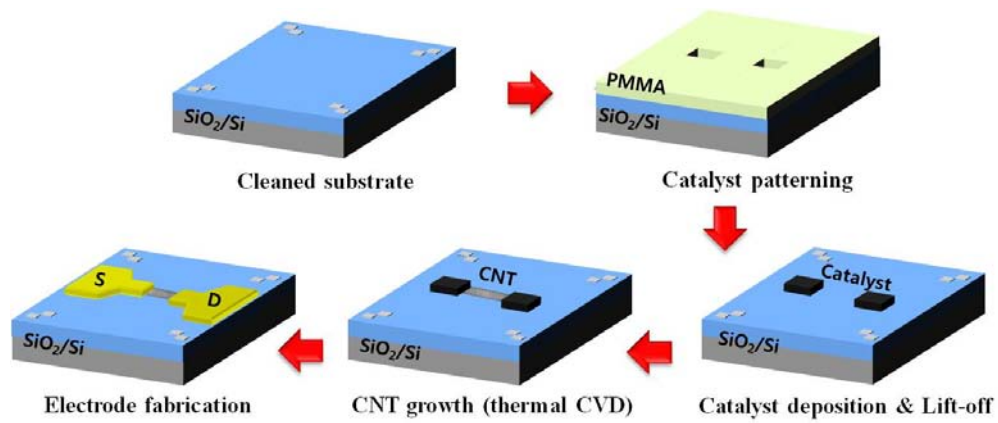
Fig. 4. 2. Schematic diagram of the carbon nanotube-field effect transistor (CNT-FET) fabrication process

Fig. 4. 3 (a) shows the scanning electron beam microscope (SEM) of grown carbon nanotube and Fe/Mo catalyst square. CNT was connected between the two catalyst pattern and straight line. Fig. 22 (b) is the atomic force microscope (AFM) image of as-grown CNT. By the AFM measurement, the diameter of CNT was about 1 nm. Source (S) and drain (D) electrical contacts to the CNT were made via electron beam lithography and thermal evaporation technique. Electrodes were made by depositing Cr/Au (5 nm /30 nm) and using a lift-off technique, followed by rapid thermal annealing (RTA) at 500 °C for 60 s in nitrogen atmosphere to form ohmic contacts.

Fig. 22 (c) is the SEM image of CNT-FET after source and drain electrode definition. After electrodes definition, we measured electrical characteristics of the CNT-FET device. Fig. 23 (a) and (b) show the source-drain current (I_{DS})-voltage (V_{DS}) and the source-drain current (I_{DS})-gate voltage (V_{BG}) curves measured in the ambient condition for the bare CNT-FET, where a heavily doped Si substrate was used as a bottom gate electrode. In the Fig 23 (a), the linear I_{DS}-V_{DS} curve confirms of ohmic contact. The CNT-FET bottom gate voltage dependence curve (Fig. 23 (b)) indicates fabricated CNT was a p-type semiconductor.
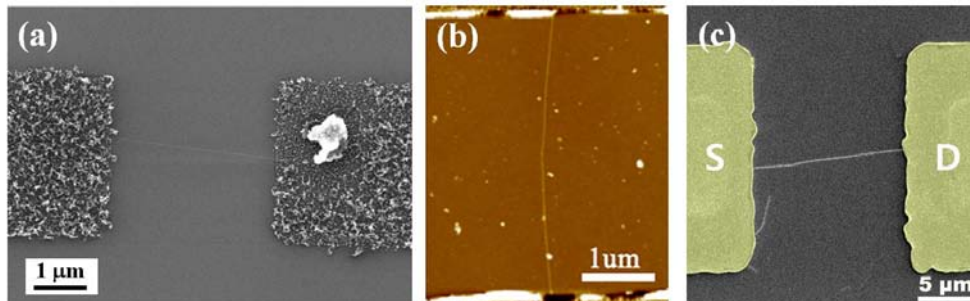
Fig. 4. 3 (a) SEM image of after CNT growth using thermal CVD (b) AFM image of as-grown CNT (c) SEM image of after source and drain electrode fabrication
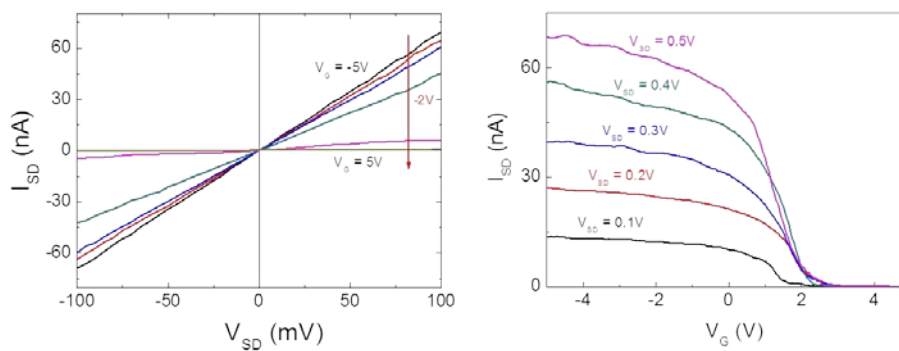
Fig. 4. 4. Electrical characteristics of single CNT-FET (a) The typical I_{DS}-V_{DS} curve with different V_G (b) The typical I_{DS}-V_{BG} curve measured with different V_{SD}

4. 3. Results and discussion

Figure 4. 5 (a) shows the I_{SD} - V_G curves measured with the source-drain voltage V_{SD}=500 mV in vacuum, 300 ppm NO_2, and 500 ppm NH_3. In vacuum, the device shows a hysteric p-type behavior as V_G is swept from -10 V to +10 V, then back to -10 V in steps of 0.04 V. Under NH_3 gas, I_{SD} is reduced and the threshold voltage is shifted to negative voltage as previously reported [106]. For NO_2, however, I_{SD} increases in the whole range of V_G and the off-state disappears. Similar disappearance of the off-state was also observed in 200 ppm NO_2 by J. Zhang, et al. [113]. The hysteresis direction is the same in all environments, i.e., positive gate voltage increases the threshold voltage, indicating that charges are injected from the CNT into the dielectric. Several groups [114, 115] also reported similar gating hysteresis and attributed it to rearrangements of charges in the substrate or in adsorbed water molecules. To see whether the observed hysteresis in NH_3 and NO_2 is caused by water molecules or gas molecules, the sensor was heated to 200°C for 30 min in vacuum and the I_{SD}-V_G curves were measured again at room temperature. As expected, the hysteresis disappeared in a vacuum. However, the hysteresis was still present under NH_3 and NO_2 environments, implying that the hysteresis in NH_3 and NO_2 is related to adsorbed gas molecules.
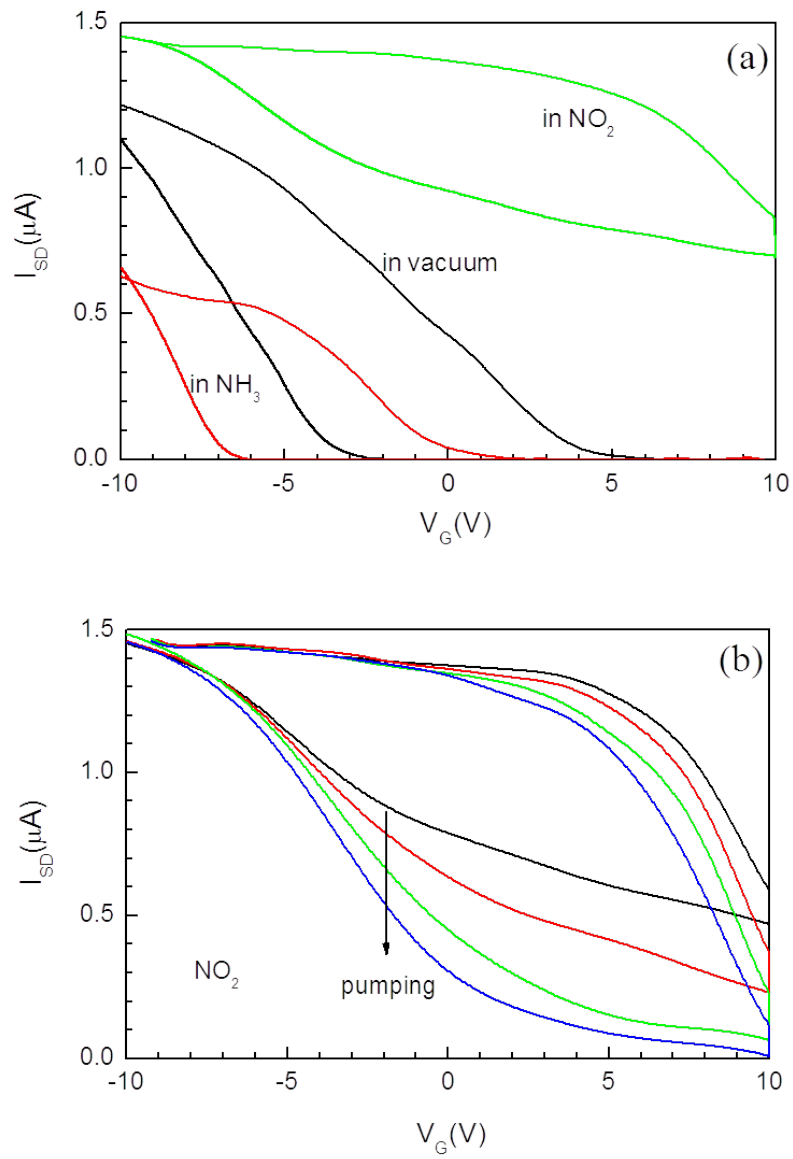
Fig. 4. 5 (a) I_{SD}-V_G curves measured with V_{SD}=500 mV in vacuum, 300 ppm NO_2, and 500 ppm NH_3. V_G is swept back and forth between -10 V and +10 V. (b) I_{SD}-V_G curves measured with V_{SD}=500 mV in different NH_3 concentrations.

Figure 4. 5(b) presents the I_{SD}-V_G curves measured while pumping NO_2 after exposing to 300 ppm NO_2. When V_G is swept from -10 V to 10 V, I_{SD} decreases as the NO_2 concentration decreases. However, when V_G is swept from 10 to -10 V, I_{SD} is relatively unchanged as the NO_2 concentration decreases, particularly at V_G = 0 V. It indicates that the negative gate voltage might affect the desorption of NO_2 molecules. It is known that NO_2 molecules are physisorbed on the CNT via dipole interactions, and electrons are transferred from the CNT to NO_2 molecules. [116] Consequently, the repulsive force induced by the negative gate voltage may weaken the binding between the CNT and NO_2 molecules and expedite the desorption of their molecules.

The result in Fig. 4. 5 (b) suggests that a gate voltage may be utilized to refresh the CNT sensor. Hence, I_{SD} was measured with V_{SD}=500 mV and V_G=0 V as a function of time, while alternately exposing the sensor to a 300 ppm NO_2 gas pulse and applying a negative gate voltage pulse (V_{Gp}) with a duration 30 s, as shown in Fig. 4. 6 (a). Indeed, when V_{Gp} is applied to the back gate, I_{SD} shows a quick transient followed by a relative steady recovery process, although I_{SD} is not fully recovered with V_{Gp}=-10 V or it is recovered after one cycle (V_{Gp} = -13 V) or four cycles (V_{Gp} = -15 V). Similar measurements were also performed under NH_3 and the results are shown in Fig. 4. 6 (b). Since NH_3 is an electron-donating molecule, a positive gate voltage pulse V_{Gp}=10 V was required to refresh the sensor in NH_3. In contrast to NO_2, I_{SD} in NH_3 recovers to the initial level without a spike upon applying V_{Gp}=10 V. These results lead to the expectation that the binding energy between gas molecules and the CNT is reduced by V_{Gp}, since that the recovery time

is given by [117]

$$\tau = \nu_o^{-1} exp(-E_B/k_B T)$$

where ν_o^{-1} is the attempt frequency, E_B the binding energy, and k_B the Boltzmann's constant. Similar gate-refreshing behavior was also observed in a ZnO nanowire-based gas sensor [116]. In the ZnO nanowire-based gas sensor, however, $V_{Gp} \approx -20$ ~ -60 V was applied to refresh the sensor in both NO_2 and NH_3.

In addition to electrically-driven gate recovery, the pronounced hysteresis reflects the memory effect. In fact, nonvolatile memory effects were reported in the CNT devices exhibiting the hysteresis. Fig. 4. 7 (a) shows the memory effects observed with our CNT sensor. In order to write or erase the state of the device, V_{Gp}=+10 or -10 V is used and its state is read with I_{SD}=500 mV and V_G=0 V in vacuum, 30 ppm and 300 ppm NH_3. During these measurements NH_3 gas was not removed unlike Fig 4. 3 (a) and (b). After V_{Gp}=10 V is applied, I_{SD} is switched to the higher current and then remains constant in vacuum. In NH_3, however, I_{SD} decays initially and remains constant after switching. Furthermore, it is noted that the decay rate k_d of I_{SD} is about -0.1 nA/s in both 30 and 300 ppm NH_3 concentrations, although the decay time is longer in 300 ppm NH_3 than in 30 ppm NH_3. This temporal response is probably due to the thermodynamic non-equilibrium state caused by V_{Gp}, since the desorption rate is temporarily enhanced by V_{Gp} as shown in Fig. 4. 7 (b). On the other hand, upon applying V_{Gp}=-10 V, I_{SD} is reduced significantly and then increases gradually in all atmospheres.
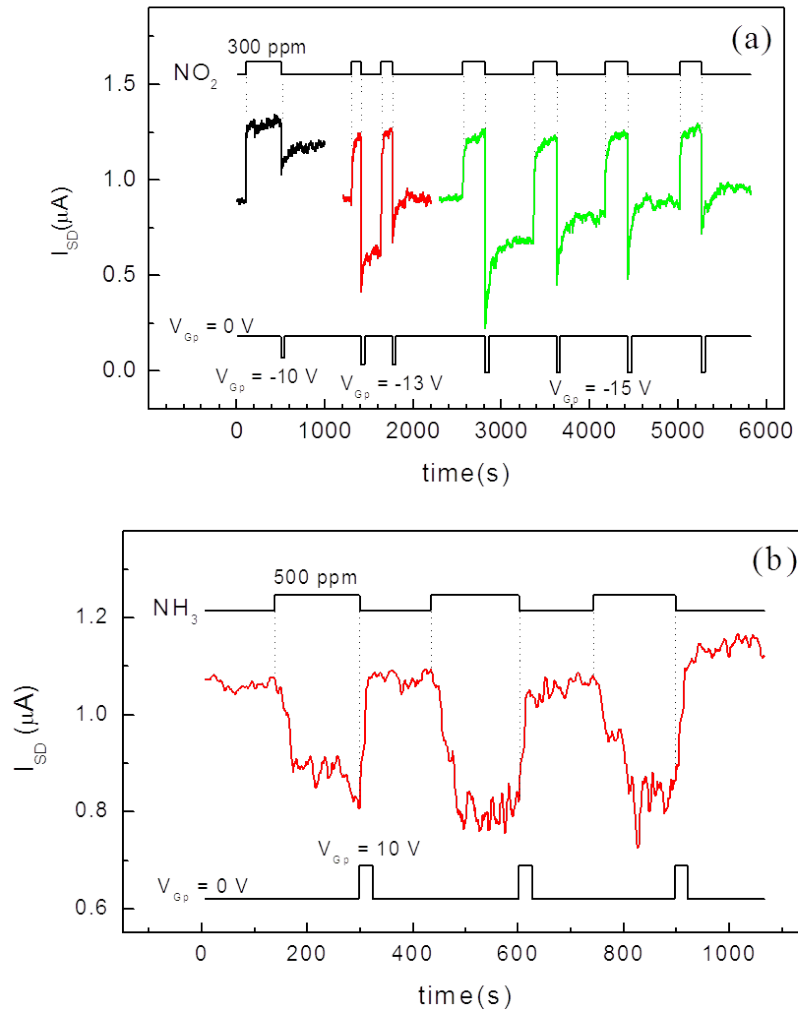
Fig. 4. 6 (a) Sensing response to 300 ppm NO_2 and the conductance recovery process caused by various V_{Gp} values . (b) Sensing response to 500 ppm NH_3 and the conductance recovery process caused by V_{Gp}=10 V. Non-volatile memory effects measured in different atmospheres.

Figure 4. 7 (b) shows the memory effect measured in different atmospheres. The initial value of I_{SD} in ethanol and benzene is much lower than that in NH_3 since I_{SD} depends on the measurement history. I_{SD} in NH_3 was measured before measuring the I_{SD}-V_G curve. However, I_{SD} in ethanol and benzene was measured after the measurement of the I_{SD}-V_G curve. Since the measurement of the I_{SD}-V_G curve induces the reduction of I_{SD} at V_G=0 V because of the hysteresis, the initial value of I_{SD} is much lower in ethanol and benzene than in NH_3. I_{SD} in ethanol and benzene exhibits similar behavior to I_{SD} in NH_3. However, k_d of I_{SD} after applying V_{Gp}=10 V is different in different gas atmosphere as shown in the inset of Fig. 4. 7 (b): $k_d \approx$ -0.1 nA/s for 30 ppm NH_3, $k_d \approx$ -0.07 nA/s for ethanol, and $k_d \approx$ -0.04 nA/s for benzene. Different k_d values are considered to be resulted from different binding energies between the CNT and the adsorbed molecules. Since k_d is found to be independent on the gas concentration in Fig. 4. 7 (a), selectivity of the sensor may be enabled by the measurement of k_d. In Fig. 4. 7 (c), the memory effects measured in NO2 are shown, and different behaviors are observed between NO_2 and NH_3.
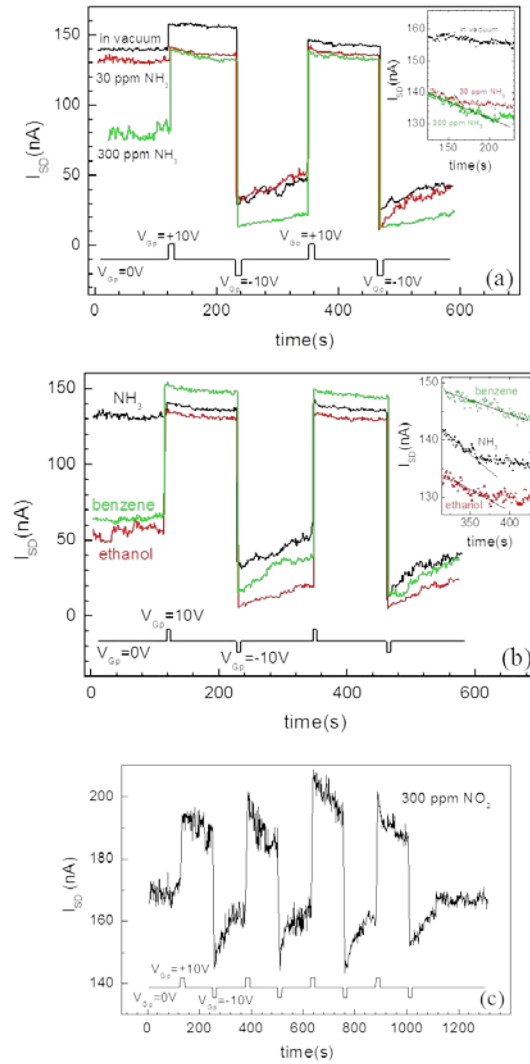
Fig. 4. 7 (a) vacuum, 30 ppm NH_3, 300 ppm NH_3; (b) 30 ppm NH_3, 1000ppm ethanol, and 15 ppm benzene; (c) 15 ppm NO_2. I_{SD} is measured as a function of time with V_{SD}=50 mV and V_G=0 V, when V_{Gp}=10 or -10 V is alternately applied to write or erase. The insets show the temporal response from t= 120 to 240 s after applying V_{Gp}=10 V in various conditions.

5. 4. Summary

This experiment was investigated the influence of gate voltage on the electrical properties of CNT chemical sensors in different atmospheres. As previously reported, the conductance of CNT decreased and the threshold voltage was shifted to the negative gate voltage in NH_3, ethanol, and benzene, whereas the conductance increases in NO_2. However, as V_G was swept back and forth between -10 V and +10 V, a clear hysteresis was observed in all atmospheres and was found to be dependent on the adsorbed molecule species and concentration, suggesting that the back-gate voltage is possibly utilized to refresh the sensor at room temperature. Indeed, I_{SD} recovered to the initial value before exposure to 300 ppm NO_2 by applying V_{Gp} = -13 V. In 500 ppm NH_3, which is an electron-donating molecule, V_{Gp} = +10 V was used to refresh the sensor. In addition, non-volatile memory effects were observed in various atmospheres and the temporal response of I_{SD} to V_{Gp} was found to be dependent on gas species, demonstrating the feasibility of distinguishing adsorbed molecules.

5. Synthesis of multilayerd nanowire using AAO template by electrodeposition

5. 1. Introduction

Spintronics burst on the scene in 1988 when French and German physicists discovered a much more powerful effect called 'giant magnetoresistance' (GMR) [118]. It results from subtle electron-spin effects in ultra-thin 'multilayers' of magnetic materials, which cause huge changes in their electrical resistance when a magnetic field is applied. GMR is 200 times stronger than ordinary magnetoresistance. IBM soon realized that read heads incorporating GMR materials would be able to sense much smaller magnetic fields, allowing the storage capacity of a hard disk to increase from 1 to 20 gigabits. In 1997 IBM launched GMR read heads, into a market worth about a billion dollars a year.

The basic GMR device consists of a three-layer sandwich of a magnetic metal such as cobalt with a nonmagnetic metal filling such as copper. A current passes through the layers consisting of spin-up and spin-down electrons. Those oriented in the same direction as the electron spins in a magnetic layer pass through quite easily while those oriented in the opposite direction are scattered. If the orientation of one of the magnetic layers can easily be changed by the presence of a magnetic field then the device will act as a filter, or 'spin valve', letting through more electrons when the spin orientations in the two layers are the same and fewer when orientations are oppositely aligned. The electrical resistance of the device can therefore be changed dramatically.

GMR structures have mostly been produced by the use of vacuum techniques such as sputtering, evaporation, and molecular beam epitaxy(MBE). But, electrodeposition has many advantages for preparing nanomeric-sized materials: the electrodeposition process is simple and relatively inexpensive; and furthermore it is a room temperature technology [119-121]. This method can also be applied for producing magnetic or nonmagnetic multilayers, including the Co-Cu system, with good GMR properties.

Numerous studies have been reported on the preparation and characterization of electrodeposited Co/Cu multilayers [122-128]. Recently. a new technique, called template synthesis, has been explored for multilayer study in the scale of nanometers [129-131]. The obtained nanomaterials consist of an array of metallic wires that are tens of nanometers in diameter. Their properties are intrinsically different from those if a bulk solid and of a multilayered film.

It is particularly useful for producing nanowires from different materials, with diameters less than 100 nm. Possible templates include nuclear tracketched polycarbonate membranes, nanochannel array glasses, mesoporous channel hosts, and self-ordered anodized aluminum oxide (AAO) films [132]. It has been found that AAO is stable at high temperature and in organic solvents, and that the pore channels in AAO films are uniform, parallel, and perpendicular to the membrane surface. This makes AAO films ideal templates for the electrodeposition of nanowire arrays. AAO films have previously been used as templates to synthesize a variety of metal and semiconductor nanowires through electrochemical processes [132-135].

Up to now, connecting a single nanowire for magnetotransport measurements was made directly during the electrodeposition process. To this end, metallic electrodes are evaporated on both sides of the membrane prior to electrodeposition. During the plating process, the emergence of the first nanowire from the membrane surface that comes into contact with the top electrode exposed to electrolytic solution is detected by a sharp increase in the deposition current [136]. The plating process is then immediately interrupted to avoid the emergence of other nanowires. Using this procedure, electrical contacts are therefore established on the two extremities of a 6~20 μm long nanowire thereby allowing two-probe measurements [137, 138]. In this paper, we will attempt that combines electrodeposition in AAO membrane and electron-beam lithography (EBL) to connect a single nanowire. Attempts were made on Co/Cu barcodes of diameters (d= 80 nm). The nanowires were grown by

electrodeposition from a sulfate bath into AAO templates. The pore sizes were 80 nm and the pore densities were close to $10^{10}/cm^2$.

5. 2. Fabrication of Co/Cu and Co/Pt nanowires

Since Masuda reported the fabrication method of anodized aluminum oxide (AAO) by using 2-step anodizing process in 1995 [132], AAO have been intensively studied because of its simple fabrication method to obtain self-assembled highly ordered nanochannel structures. AAO is consisted of tunable nanometer-sized pore arrays surrounded by an alumina backbone. AAO has been used as a template for growth of many kinds of nanowires (NWs) [133] or nanotube (NTs) [134], because of its possibilities to integrate various nanowires. AAO has a hexagonally packed columnar structure with cylindrical, uniformly sized pores ranging from 10 to 200 nm in diameter [135]. AAO membrane is very promising material because nanopores are well ordered hexagonal structure which is difficult to form by a conventional lithographic technique.

To obtain highly ordered AAO template, Al films were anodized by 2-step anodizing process. 2-step anodization process was well-known for better pore arrangement. Fig. 5. 1 shows the schematic flow diagram of 2-step anodization process. 2-step anodization process consists of several steps. The first step is electropolishing step which smoothen Al surface to improve the arrangement of nanopore. Without this step, non-uniform electric field due to irregular electrolyte/Al interface results in non-uniform nanopore penetration.
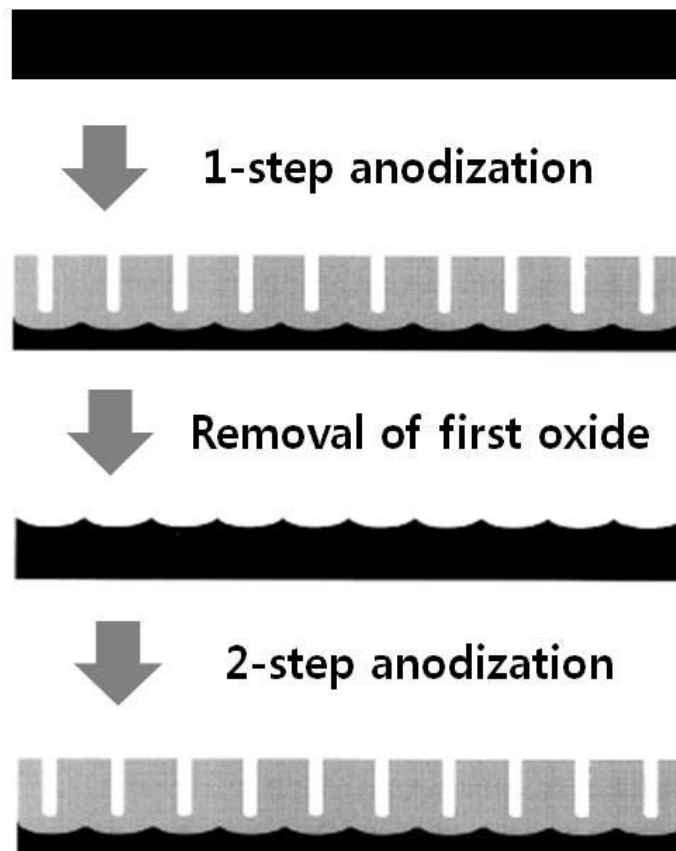
Fig. 5. 1. Experimental procedures of 2-step anodization.

The second step is 1st anodization process to fabricate AAO layers. However, the AAO layer fabricated from this step has a poor pore arrangement. Next two steps are chemical etching of the AAO layer and 2nd anodization step. After removing the alumina layer which has poor nanopore arrangement, hexagonally well-ordered AAO layer is formed through 2nd anodization step.

The 2-step anodization process was performed by following step. Al foils (Sigma-Aldrich, 99.999 %) were used as the starting material. Al foils were electrochemical polished with a mixed solution of 1:5 v/v ($HClO_4/C_2H_5OH$). Al foils were anodized under constant voltage 40 V in 0.3 M oxalic acid ($C_2H_2O_4$) for 6 h which was held at 0°C. The AAO layers were dissolved in a mixed solution of 1.8 wt% H_2CrO_4 and 6 wt% H_3PO_4 at 60°C for 6 h. These textured Al specimens were anodized again for 12 h under same conditions used in the first anodizing step. The AAO templates were detached from Al foil at 45 V in 1:1 v/v ($HClO_4/C_2H_5OH$) solution [139], and then the barrier layer was removed in 6 wt % H_3PO_4 solution during 40 min at 30°C. After barrier removing process, the diameter of AAO nanopore is widened from 50 to 70 nm. A 300 nm-thick gold (Au) or copper (Cu) layer was sputtered on to one side of the AAO template to provide a conducting film. Fig. 5. 2 shows the FESEM image of a fabricated AAO template.
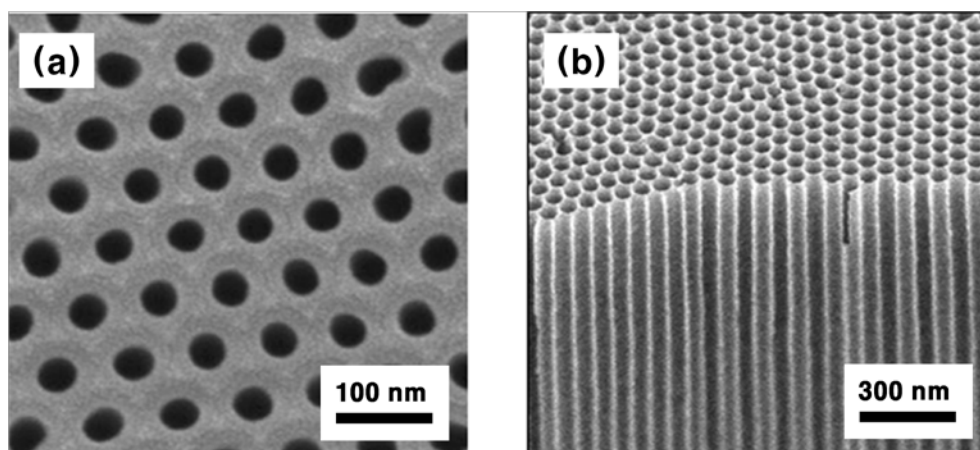
Fig. 5. 2. FESEM images of a fabricated (a) top and (b) side view of AAO membrane, respectively.

Multilayered magnetic nanowires were prepared by pulsed electrodepositing Co/Cu and Co/Pt in the pores of AAO templates. For electrodeposition of Co/Cu and Co/Pt, a 300 nm-thick Au film was deposited onto one side of the AAO template. Pulsed electrochemical deposition in one bath containing both Co^{2+} and Cu^{2+} or Pt^{2+} ion was used for the synthesis of Co/Cu or Co/Pt nanowires. The electrochemical deposition was performed via a 3-electrode method. Pt wire is chosen to be counter electrode and the Ag/AgCl electrode (in 3.5M KCl solution) is the reference electrode. The experimetical reduction potential of Co and Cu or Pt is found to be -1000 mV (v.s.Ag/AgCl) and -540 mV or -350 mV(v.s. Ag/AgCl) respectively. The sulfates of Co and Cu are chosen as the sources of metal ions and also the chloroplatinate was chosen as the source of Pt ions. The concentration ratio of $CoSO_4$ or $CuSO_4/K_2Pt_4Cl_6$ is set at 100 to 1 in order to decrease the rate of Cu/Pt reduction during deposition of Co. The concentration of $CoSO_4$ and $CuSO_4/$

K$_2$PtCl$_6$ are 1 M and 0.01 M respectively. The time of each pulse can be changed to tune the thickness of each layer. After the nanowires were formed, the gold electrode was removed by reactive ion etching and then the AAO was dissolved in 6 M NaOH to achieve Co/Cu and Co/Pt nanowires. These nanowires were analyzed using SEM (JSM-6500F, JEOL) and EDX (attatched SEM) to obtain the morphology and composition. VSM were used to characterize the magnetic properties of these nanowires. Single nanowire devices for MR measurement were fabricated using by e-beam lithography and lift-off technique.

5. 3. Result and discussion

Fig. 5. 3 (a) shows the schematic diagram of fabrication of multilayer nanowires. Co/Cu multilayered nanowires were deposited with Co segments. Fig. 5. 3 (b) shows SEM images of Co/Cu multilayered nanowires before and after removing of AAO template. The existence of rigid structure without dissolved region confirms that the nanowires were successfully synthesized. The diameter of nanowires is about 60 nm, slightly larger than the nanowires inside the AAO (~ 55 nm). It is because the surface of nanowires was slightly oxidized by NaOH during the AAO template removing process.
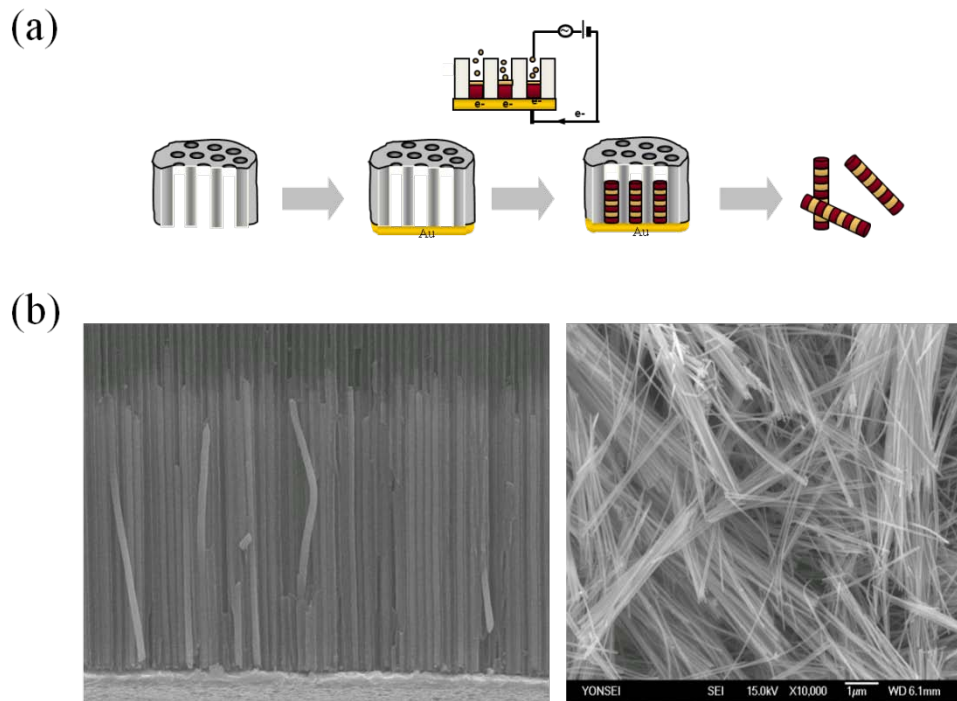
Fig. 5. 3. (a) Schematic diagram of multilayered nanowires (b) FESEM images of a fabricated Co/Cu multilayered nanowire before and after removing AAO template.
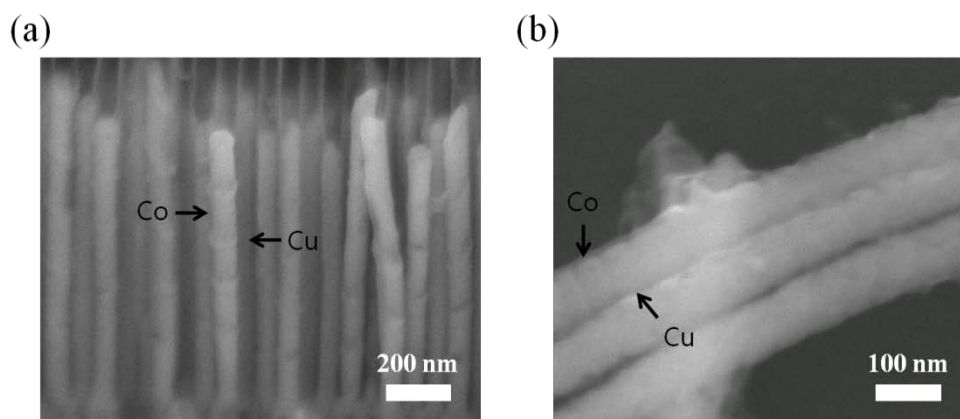

Fig. 5. 4. FESEM images of a fabricated Co/Cu multilayered nanowire with various layers (a) 5 (b) 50

Fig. 5. 4 shows the bamboo-like layered structure with (a) 5 (b) 50 layers, respectively. The reproducibility of the layer thickness are clearly seen. The multilayered nanowires are highly regular and uniform, with an average diameter of about 65 nm, which corresponds closely to the nanochannel size. Any desired nanowires with different sequences and thicknesses can be easily fabricated by simply changing the programmable deposition conditions.

Fig. 5. 5 shows the X-ray spectroscopy (EDS) spectrum of detached Co/Pt nanowires on SiO2/Si substrate. It can be detected clearly Cobalt and Platinum element. Fig. 5. 6 shows X-ray spectroscopy (EDS) mapping and line profile of Co/Cu multilayered nanowires with (a) 2 layers and (b) 4 layers inside AAO template. These data ware able to confirm that multilayered nanowier is well-formed clearly.

The properties of the Co/Cu magnetic multilayered nanowires including magnetic properties, such as coercivity and remanence. The external field was applied parallel (//) and perpendicular (^) to the axes of the nanowires. The magnetic behavior of high aspect ratio multilayered nanowires (aspect ratio of ferromagnetic layer > 1) show that an easy axis is parallel to the nanowire axis (Fig. 5. 7), as can be elucidated from the large coercivity and remanence values while low aspect ratio magnetic multilayered nanowires show an easy axis is perpendicular to the nanowires axis . In the latter case, the coercivity and remanence values are small when the applied field is both parallel and perpendicular to the nanowires. The results indicate that the coercivity of the nanowires initially increases rapidly with an increase in the aspect ratio of the cobalt segments but then approaches saturation.

Similar observations were reported in the case of pure cobalt nanowires. Our observation of modulated magnetism in the Co/Cu multilayered nanowires corresponding to the aspect ratio change indicates that the magnetic properties of multilayered nanowires can be easily tuned by controlling the relative thickness of the cobalt segments in the Co/Cu magnetic multilayered nanowires.

The magneto-transport properties were investigated by the Quantum Design Physical Property Measurement System (PPMS) with the sketch of the measurement setup in the inset Fig. 5. 8. The measurement of the magneto-resistance is performed with the applied magnetic field perpendicular to the long axis. In the arrangement the electric current is perpendicular to the applied magnetic field. The calculation of the magnetoresistance (MR) is performed with the formula

$$MR = \frac{R_H - R_0}{R_0} \times 100 \text{ \%}$$

where R(H) and R0 represent the resistance with and without a magnetic field, respectively [122, 123].

The obtained MR curves are mainly attributed to the anisotropic magneto-resistance (AMR) in low-dimensional systems. The AMR is caused by an anisotropic scattering of electrons with strong dependence on the orientation of the external magnetic field relative to the current direction. This consequence originates from the spin-orbit interaction.
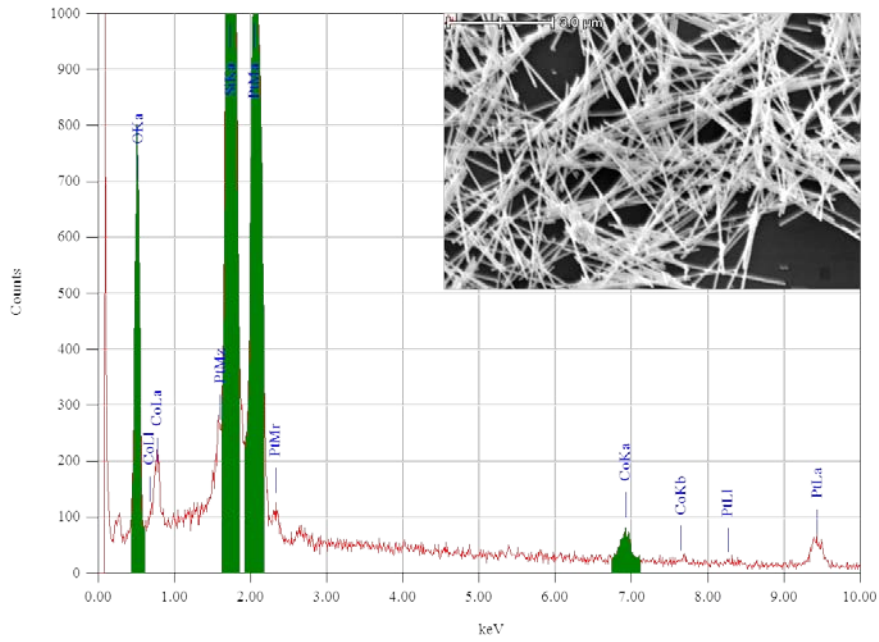
Fig. 5. 5. Energy dispersive X-ray element spectrum of a Co/Pt multilayered nanowire.

(a)

SEM　　　　　Cobalt　　　　　Copper　　　　Line profile

(b)

SEM　　　　　Cobalt　　　　　Copper　　　　Line profile
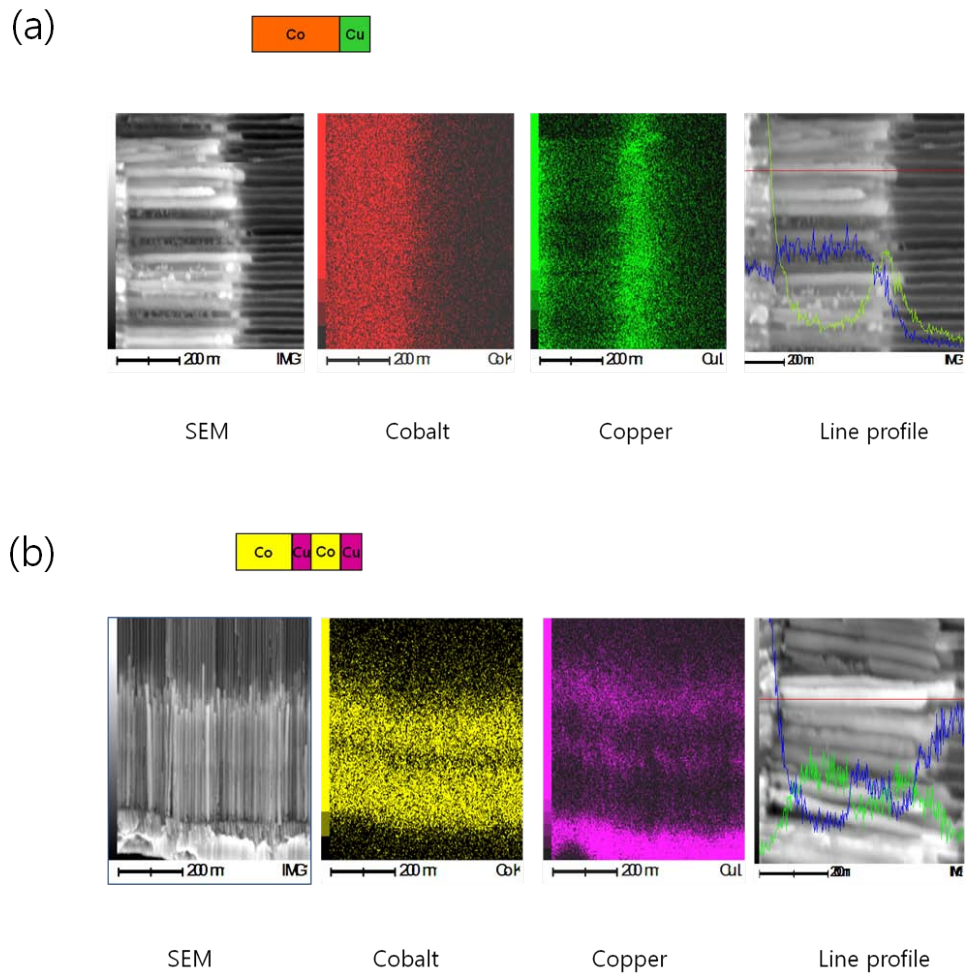
Fig. 5. 6. Energy dispersive X-ray mapping and line profile of a Co/Cu multilayered nanowire (a) 2 layers (b) 4 layers.

(a)
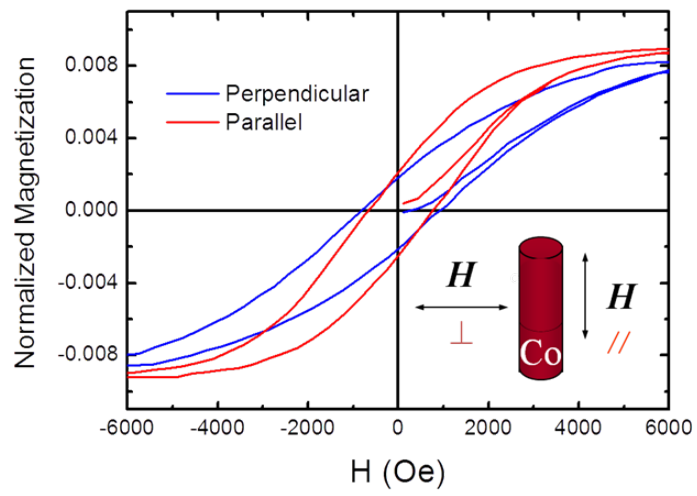
(b)
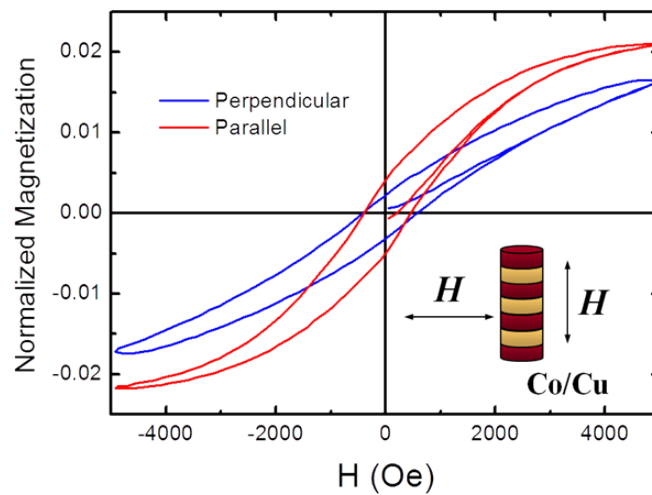
Fig. 5. 7. Magnetic hysteresis loops (a) pure Co nanowires and (b) Co/Cu multilayered nanowires at 300 K with applied field perpendicular to the nanowires (blue line) and parallel to the nanowires (red line). The nanowire diameter is about 60 nm.
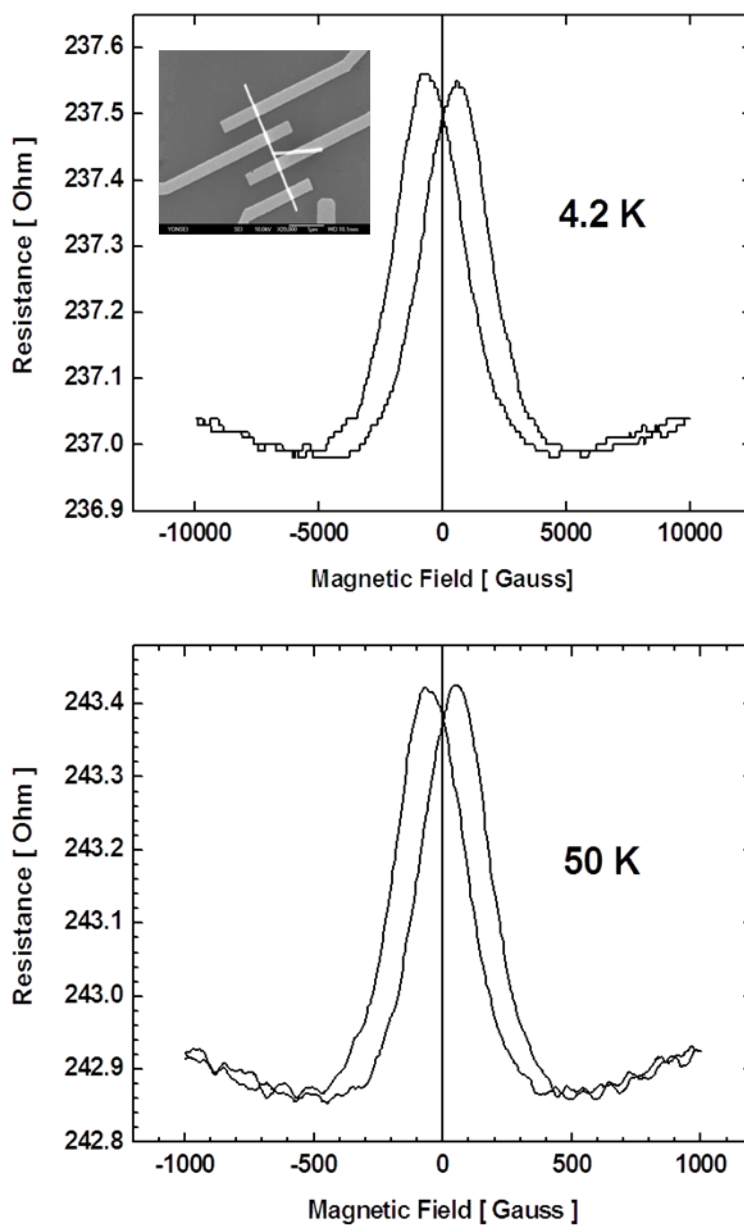
Fig. 5. 8. Magneto-resistance of Co/Pt single nanowire, with the current applied on the longitudinal axis of the Co/Pt NWs and perpendicular to the applied magnetic field. Inset, SEM image of 4 point contact single nanowire.

5. 4. Summary

Various size and composition of magnetic Co/Cu and Co/Pt multilayered nanowire were fabricated via pulsed-electrodeposition method into a AAO templates (pore diameter; 80 nm) A single multilayered nanowire was isolated and their magnetoelectronic properties were investigated. When extended magnetic field was applied, increase of resistance was observed comparing to zero-magnetic field resistance of the multilayered nanowire. Further study will be performed such as, layer thickness, repeated number of layers. Our study is the first observation of magnetic properties of a magnetic single multilayered nanowires and will be a foundation for understanding the relationship between magnetic spins and electronic transport in a single nanowire level.

Reference

[1] W. H. Coulter, *U. S. Patent*, 2656508 (1953)

[2] J. J. Kasianowicz, E. Brandin, D. Branton, and D. W. Deamer, *Proc. Natl. Acad. Sci. USA,* **93**, 13770-13773 (1996)

[3] S. Bhakdi, R. Fussle and J. Tranum-Jensent, *Proc. Natl. Acad. Sci. USA,* **78**, 5475-5479 (1981)

[4] H. Bayley, *Bioorg. Chem.*, **23**(4), 340-354 (1995)

[5] L. Song, M. R. Hobaugh, C. Shustak, S. Cheley, H. Bayley and J. E. Gouaux, *Science*, **274**, 1859-1865 (1996)

[6] J. J. Kasianowicz, D. L. Burden, L. C. Han, S. Cheley and H. Bayley, *Biophys. J.*, **76**, 837-845 (1999)

[7] G. Menestrina, *J. Membrane Biol.*, **90**, 177-190 (1986)

[8] M. Akeson, D. Branton, J. J. Kasianowicz, E. Brandin and D. W. Deamer, *Biophys. J.*, **77**, 3227-3233 (1999)

[9] S. M. Bezrukov and J. J. Kasianowicz, *Phys. Rev. Lett.*, **70**, 2352-2355 (1993)

[10] J. J. Kasianowicz and S. M. Bezrukov, *Biophys. J.*, **69**, 94-105 (1995)

[11] M. Misakian and J. J. Kasianowicz, *J. Membrane Biol.*, **195**, 137-146 (2003)

[12] P. G. Merzlyak, M. F. Capistrano, A. Valeva, Kasianowicz and O. V. Krasilnikov, *Biophys. J.*, **89**, 3059-3070 (2005)

[13] Y. E. Korchev, C. L. Bashford, G. M. Alder, J. J. Kasianowicz and C. A. Pasternak, *J. Membrane Biol.*, **147**, 233-239 (1995)

[14] C. L. Bashford, G. M. Alder, J. M. Graham, G. Menestrina and C. A. Pasternak, *J. Membrane Biol.*, **103**, 79-94 (1988).

[15] A. W. Bernheimer, L. S. Avigad and G. Avigad, *Infect. Immun.*, **11**, 1312-1319 (1975)

[16] S. P Howard, W. J. Garland, M. J. Green and J. T. Buckley, *J. Bacteriol.*, **169**, 2869-2871 (1987).

[17] Howard, S.P., and Buckley, J.T. (1985) J Bacteriol *163*, 336-340

[18] F. G. van der Goot, J. Ausio, K. R. Wong, F. Pattus and J. T. Buckley, *J. Biol. Chem.*, **268**, 18272-18279 (1993)

[19] M. Moniatte, F. G. van der Goot, J. T. Buckley, F. Pattus and A. van Dorsselaer, *FEBS Lett.* **384**, 269-272 (1996)

[20] M. Fivaz, M. C. Velluz and F. G. van der Goot, *J. Biol. Chem.* **274**, 37705-37708 (1999)

[21] M. W. Parker, J. T. Buckley, J. P. Postma, A. D. Tucker, K. Leonard, F. Pattus, and D. Tsernoglou, *Nature* **367**, 292-295 (1994)

[22] H. U. Wilmsen, K. R. Leonard, W. Tichelaar, J. T. Buckley and F. Pattus, *EMBO. J.* **11**, 2457-2463 (1992)

[23] H. U. Wilmsen, F. Pattus and J. T. Buckley, *J. Membr. Biol*. **115**, 71-81 (1990)

[24] H. U. Wilmsen, J. T. Buckley and F. Pattus, *Mol. Microbiol.* **5**, 2745-2751 (1991)

[25] R. Stefureac, Y. T. Long, H. B. Kraatz, P. Howard and J. S. Lee, *Biochemistry* **45**, 9172-9179 (2006)

[26] M. Pastoriza-Gallego, G. Oukhaled, J. Mathe, B. Thiebot, J. M. Betton, L. Auvray and J. Pelta, *FEBS Lett.* **581**, 3371-3376 (2007)

[27] M. Pastoriza-Gallego, L. Rabah, G. Gibrat, B. Thiebot, F. G. van der Goot, L. Auvray, J. M. Betton and J. Pelta, *J. Am. Chem. Soc.* **133**, 2923-2931 (2011)

[28] C. Stahl, S. Kubetzko, I. Kaps, S. Seeber, H. Engelhardt and M. Niederweis, *Mol. Microbiol.* **40**, 451-464 (2001)

[29] M. Niederweis, S. Ehrt, C. Heinz, U. Klocker, S. Karosi, K. M. Swiderek, L. W. Riley and R. Benz, *Mol. Microbiol.* **33**, 933-945 (1999)

[30] M. Faller, M. Niederweis and G. E. Schulz, *Science* **303**, 1189-1192 (2004)

[31] T. Z. Butler, M. Pavlenok, I. M. Derrington, M. Niederweis and J. H. Gundlach, *Proc. Natl. Acad. Sci. USA* **105**, 20647-20652 (2008)

[32] T. C. Sutherland, Y. –T. Long, R. –I. Stefureac, I. Bediako-Amoa, H. –B Kraatz and J. S. Lee, *Nano Lett.* **4**, 1273-1277 (2004)

[33] R. Stefureac, L. Waldner, P. Howard and J. S. Lee, *Small* **4**, 59-63 (2008)

[34] J. Li, D. Stein, C. McMullan, D. Branton, M. J. Aziz and J. A. Golovchenko, *Nature* **412**, 166-169 (2001)

[35] D. Stein, J. Li and J. A. Golovchenko, *Phys. Rev. Lett.* **89**, 276106 (2002)

[36] T. Mitsui, D. Stein, Y. R. Kim, D. Hoogerheide and J. A. Golovchenko, *Phys. Rev. Lett.* **96**, 036102 (2006)

[37] P. Chen, T. Mitsui, D. B. Farmer, J. A. Golovchenko, R. G. Gordon and D. Branton, *Nano Lett.* **4**, 1333-1337 (2004)

[38] D. Stein, M. Kruithof and C. Dekker, *Phys. Rev. Lett.* **93**, 035901 (2004)

[39] A. J. Storm, J. H. Chen, X. S. Ling, H. W. Zandbergen and C. Dekker, *Nat. Mater.* **2**, 537-540 (2003)

[40] M. J. Kim, M. Wanunu, D. C. Bell and A. Meller, *Adv. Mater.* **18**, 3149-3153 (2006)

[41] M. J. Kim, B. McNally, K. Murata and A. Meller, *Nanotechnology* **18**, 205302 (2007)

[42] V. Tabard-Cossa, D. Trivedi, M. Wiggin, N. N. Jetha1 and A. Marziali1, *Nanotechnology* **18**, 305505 (2007)

[43] S. Garaj, W. Hubbard, A. Reina, J. Kong, D. Branton and J. A. Golovchenko, *Nature* **467**, 190-193 (2010)

[44] C. A. Merchant, K. Healy, M. Wanunu, V. Ray , N. Peterman, J. Bartel, M. D. Fischbein, K. Venta, Z. Luo, A. T. C. Johnson and M. Drndić, *Nano Lett.* **10**, 2915-2921 (2010)

[45] G. F. Schneider, S. W. Kowalczyk, V. E. Calado, G. Pandraud, H. W. Zandbergen, L. M. Vandersypen and C. Dekker, *Nano Lett*. **10**, 3163-3167 (2010)

[46] R. L. Fleischer and P. B. Price, *Science* **140**, 1221-1222 (1963)

[47] P.Y. Apel, Y. E. Korchev, Z. Siwy, R. Spohr and M. Yoshida, *Nuclear Instruments and Methods in Physics Research Section B: Beam Interactions with Materials and Atoms* **184**, 337-346 (2001)

[48] Z. Siwy, Y. Gu, H. A. Spohr, D. Baur, A. Wolf-Reber, R. Spohr, P. Apel and Y. E. Korchev, *Europhys. Lett.* **60**, 349-355 (2002)

[49] Z. Siwy, D. Dobrev, R. Neumann, C. Trautmann and K. Voss, *Applied Physics A: Materials Science & Processing* **76**, 781-785 (2003)

[50] Z. Siwy, P. Apel, D. Dobrev, R. Neumann, R. Spohr, C. Trautmann and K. Voss, *Nuclear Instruments and Methods in Physics Research Section B: Beam Interactions with Materials and Atoms* **208**, 143-148. (2003)

[51] J. E. Wharton, P. Jin, L. T. Sexton, L. P. Horne, S. A. Sherrill, W. K. Mino and C. R. Martin, *Small* **3**, 1424-1430 (2007)

[52] H. Daiguji, Y. Oka and K. Shirono, *Nano Lett.* **5**, 2274-2280 (2005)

[53] Z. Siwy, *Adv. Func. Mater.* **16**, 735-746 (2006)

[54] R. M. M. Smeets, U. F. Keyser, M. Y. Wu, N. H. Dekker and C. Dekker, *Phys. Rev. Lett.* **97**, 088101 (2006)

[55] L. T. Sexton, L. P. Horne, S. A. Sherrill, G. W. Bishop, L. A. Baker and C. R. Martin, *J. Am. Chem. Soc.* **129**, 13144-13152 (2007)

[56] M. Wanunu and A. Meller, *Nano Lett.* **7**, 1580-1585 (2007)

[57] E. C. Yusko, J. M. Johnson, S. Majd, P. Prangkio, R. C. Rollings, J. Li, J. Yang and M. Mayer, *Nat. Nanotechnol.* **6**, 253-260 (2011)

[58] A. Meller, L. Nivon, E. Brandin, J. Golovchenko and D. Branton, *Proc. Natl. Acad. Sci. USA* **97**, 1079-1084 (2000)

[59] W. Vercoutere, S. Winters-Hilt, H. Olsen, D. Deamer, D. Haussler and M. Akeson, *Nat. Biotechnol.* **19**, 248-252 (2001)

[60] W. A. Vercoutere, S. Winters-Hilt, V. S. DeGuzman, D. Deamer, S. E. Ridino, J. T. Rodgers, H. E. Olsen, A. Marziali and M. Akeson, *Nucleic Acids Res.* **31**, 1311-1318 (2003)

[61] S. Winters-Hilt, W. A. Vercoutere, V. S. DeGuzman, D. Deamer, M. Akeson and D. Haussler, *Biophys. J.* **84**, 967-976 (2003)

[62] J. Mathe, H. Visram, V. Viasnoff, Y. Rabin and A. Meller, *Biophys. J.* **87**, 3205-3212 (2004)

[63] J. Nakane, M. Wiggin and A. Marziali, *Biophys. J.* **87**, 615-621 (2004)

[64] N. Mitchell and S. Howorka, *Angew. Chem. Int. Ed. Engl.* **47**, 5565-5568 (2008)

[65] V. Borsenberger, N. Mitchell and S. Howorka, *J. Am. Chem. Soc.* **131**, 7530-7531 (2009)

[66] R. S. S. de Zoysa, D. A. Jayawardhana, Q. Zhao, D. Wang, D. W. Armstrong and X. Guan, *J. Phys. Chem. B* **113**, 13332-13336 (2009)

[67] M. Rincon-Restrepo, E. Mikhailova, H. Bayley and G. Maglia, *Nano Lett.* **11**, 746-750 (2011)

[68] S. E. Henrickson, M. Misakian, B. Robertson and J. J. Kasianowicz, *Phys. Rev. Lett.* **85**, 3057-3060 (2000)

[69] T. Z. Butler, J. H. Gundlach and M. A. Troll, *Biophys. J.* **90**, 190-199 (2006)

[70] A. Meller, L. Nivon and D. Branton, *Phys. Rev. Lett.* **86**, 3435-3438 (2001)

[71] C. Dekker, *Nat. Nanotechnol.* **2**, 209-215 (2007)

[72] D. Branton, D. W. Deamer, A. Marziali, H. Bayley, S. A. Benner, T. Butler, M. Di Ventra, S. Garaj, A. Hibbs, X. Huang, S. B. Jovanovich, P. S. Krstic, S. Lindsay, X. S. Ling, C. H. Mastrangelo, A. Meller, J. S. Oliver, Y. V. Pershin, J. M. Ramsey, R. Riehn, G. V. Soni, V. Tabard-Cossa, M. Wanunu, M. Wiggin, J. A. Schloss, *Nat. Biotechnol.* **26**, 1146-1153 (2008)

[73] Y. Astier, O. Braha and H. Bayley, *J. Am. Chem. Soc.* **128**, 1705-1710 (2006)

[74] J. Clarke, H. C. Wu, L. Jayasinghe, A. Patel, S. Reid and H. Bayley, *Nat. Nanotechnol.* **4**, 265-270 (2009)

[75] S. L. Cockroft, J. Chu, M. Amorin and M. R. Ghadiri, *J. Am. Chem. Soc.* **130**, 818-820 (2008)

[76] B. Gyarfas, F. Olasagasti, S. Benner, D. Garalde, K. R. Lieberman and M. Akeson, *ACS Nano* **3**, 1457-1466 (2009)

[77] N. Hurt, H. Wang, M. Akeson and K. R. Lieberman, *J. Am. Chem. Soc.* **131**, 3772-3778 (2009)

[78] N. A. Wilson, R. Abu-Shumays, B. Gyarfas, H. Wang, K. R. Lieberman, M. Akeson and W. B. Dunbar, *ACS Nano* **3**, 995-1003 (2009)

[79] J. Chu, M. Gonzalez-Lopez, S. L. Cockroft, M. Amorin and M. R. Ghadiri, *Angew. Chem. Int. Ed. Engl.* **49**, 10106-10109 (2010)

[80] K. R. Lieberman, G. M. Cherf, M. J. Doody, F. Olasagasti, Y. Kolodji and M. Akeson, *J. Am. Chem. Soc.* **132**, 17961-17972 (2010)

[81] F. Olasagasti, K. R. Lieberman, S. Benner, G. M. Cherf, J. M. Dahl, D. W. Deamer and M. Akeson, *Nat. Nanotechnol.* **5**, 798-806 (2010)

[82] K. R. Garalde, C. A. Simon, J. M. Dahl, H. Wang, M. Akeson and K. R. Lieberman, *J. Biol. Chem.* **286**, 14480-14492 (2011)

[83] D. Stoddart, A. J. Heron, E. Mikhailova, G. Maglia and H. Bayley, *Proc. Natl. Acad. Sci. USA* **106**, 7702-7707 (2009)

[84] D. Stoddart, G. Maglia, E. Mikhailova, A. J. Heron and H. Bayley, *Angew. Chem. Int. Ed. Engl.* 49, 556-559 (2010)

[85] E. V. Wallace, D. Stoddart, A. J. Heron, E. Mikhailova, G. Maglia, T. J. Donohoe and H. Bayley, *Chem. Comm.* **46**, 8195-8197 (2010)

[86] I. M. Derrington, T. Z. Butler, M. D. Collins, E. Manrao, M. Pavlenok, M. Niederweis and J. H. Gundlach, *Proc. Natl. Acad. Sci. USA* **107**, 16060-16065 (2010)

[87] J. Li, M. Gershow, D. Stein, E. Brandin and J. A. Golovchenko, *Nat. Mater.* **2**, 611-615 (2003)

[88] D. Fologea, M. Gershow, B. Ledden, D. S. McNabb, J. A. Golovchenko and J. Li, *Nano Lett.* **5**, 1905-1909 (2005)

[89] A. J. Storm, C. Storm, J. Chen, H. Zandbergen, J. F. Joanny and C. Dekker, *Nano Lett. 5*, 1193-1197 (2005)

[90] M. Wanunu, B. Chakrabarti, J. Mathe, D. R. Nelson and A. Meller, *Phys. Rev. E* **77**, 031904 (2008)

[91] D. Fologea, E. Brandin, J. Uplinger, D. Branton, D and J. Li, *Electrophoresis* **28**, 3186-3192 (2007)

[92] D. Fologea, J. Uplinger, B. Thomas, D. S. McNabb and J. Li, *Nano Lett.* **5**, 1734-1737 (2005)

[93] B. McNally, A. Singer, Z. Yu, Y. Sun, Z. Weng and A. Meller, *Nano Lett.* **10**, 2237-2244 (2010)

[94] Q. Zhao, J. Comer, V. Dimitrov, S. Yemenicioglu, A. Aksimentiev and G. Timp, *Nucleic Acids Res.* **36**, 1532-1541(2008)

[95] M. Zwolak and M. Di Ventra, *Nano Lett.* **5**, 421-424 (2005)

[96] M. E. Gracheva, A. Xiong, A. Aksimentiev, K. Schulten, G. Timp and J. –P Leburton, *Nanotechnology* **17**, 622-633 (2006)

[97] J. Lagerqvist, M. Zwolak and M. Di Ventra, *Nano Lett.* **6**, 779-782 (2006)

[98] J. Lagerqvist, M. Zwolak and M. Di Ventra, *Biophys. J.* **93**, 2384-2390 (2007)

[99] X. Liang and S. Y. Chou, *Nano Lett.* **8**, 1472-1476 (2008)

[100] M. Tsutsui, M. Taniguchi and T. Kawai, *Nano Lett.* **9**, 1659-1662 (2009)

[101] B. McNally, A. Singer, Z. Yu, Y. Sun, Z. Weng and A. Meller, *Nano Lett.* **10**, 2237-2244 (2010)

[102] A. R. Hall, A. Scott, D. Rotem, K. K. Mehta, H. Bayley and C. Dekker, *Nat. Nanotechnol.* **5**, 874-877 (2010)

[103] B. Venkatesan, J. Polans, J. Comer, S. Sridhar, D. Wendell, A. Aksimentiev and R. Bashir, *Biomedical Microdevices* **13**, 671-682 (2011)

[104] L. J. Steinbock, O. Otto, C. Chimerel, J. Gornall and U. F. Keyser, Nano Lett. 10, 2493-2497 (2010)

[105] S. Hern´andez-Ainsa, C. Muus, N. A.W. Bell, L. J. Steinbock, V. V. Thackera and U. F. Keyser, Analyst 138, 104-106 (2013)

[106] J. Kong, N. Franklin, C. Zhou, M. Chapline, S. Peng, K. Cho and H. Dai, *Science* **287**, 622 (2000)

[107] E. S. Snow, F. K. Perkins, E. J. Houser, S. C. Badesu and T. L. Reinecke, *Science* **307**, 1942 (2005)

[108] C. Li, D. Zhang, X. Liu, S. Han, T. Tang, J. Han and C. Zhou, *Appl. Phys. Lett.* **82**, 1613 (2003)

[109] W.-S. Cho, S.-I. Moon, Y.-D. Lee, Y.-H. Lee, J.-H. Park, B. W. Ju, *IEEE Electron Dev. Lett.* **26**, 498 (2005)

[110] A. Star, T.-R. Han, V. Joshi, J.-C. P. Gabriel and G. Grüner, *Adv. Mater.* **16**, 2040 (2004)

[111] P. Qi, O. Vermesh, M. Grecu, A. Javey, Q. Wang and H. Dai, *Nano Lett.* **3**, 347 (2003)

[112] J. Kong, H. T. Soh, A. M. Cassell, C. F. Quate and H. Dai, *Naure* **395**, 878 (1998)

[113] J. Zhang, A. Boyd, A. Tselev, M. Paranjape and P. Barbara, *Appl. Phys. Lett.* **88**, 123112 (2006)

[114] M. S. Fuhrer, B. M. Kim, T. Dürkop and T. Bringtlinger, *Nano Lett.* **2**, 755 (2002)

[115] W. Kim, A. Javey, O. Vermesh, Q. Wang, Y. Li, H. Dai, *Nano Lett.* **3**, 193 (2003)

[116] S. Peng, K. Cho, P. Qi, H. Dai, *Chem. Phys. Lett.* **387**, 271 (2004)

[117] Z. Fan and J. G. Lu, *Appl. Phys. Lett.* **86**, 123510 (2005)

[118] M. N. Baibich, J. M. Broto, A. Fert, F. Nguyen Van Dau, F. Petroff, P. Eitenne, G. Creuzet, A. Friederich and J. Chazelas, Phys. Rev. Lett. 61, 2472-2475 (1988)

[119] C. R. Martin, Science 266, 1961-1966 (1994)

[120] J. C. Hulteen and C. R. Martin, *J. Mater. Chem.* **7**, 1075−1087 (1997)

[121] C. R. Martin and D. T. Mitchell, *Anal. Chem.* **70**, 322A-327A (1998)

[122] L. Piraux, J.M. George, J.F. Despres, C. Leroy, E. Ferain, G. Legras, K.

Ounadjela and A. Fert, *Appl.Phys. Lett.* **65**, 2484 (1994)

[123] A. Blondel, J.P. Meir, B. Doudin and J.-Ph. Ansermet, *Appl. Phys. Lett.* **65**, 3020 (1994)

[124] K. Liu, K. Nagodawithana, P.C. Pearsin and C.L Chein, *Phys. Rev. B.* **51**, 7381 (1995)

[125] L. Gravier, A. Fabian, A. Rudolf, A. Cachin, J.-E. Wegrowe and J.-Ph. Ansermet, *J. Magn. Magn. Mater.* **271**, 153 (2004)

[126] B. Voegeli, A. Blondel, B. Doudin and J.-Ph. Ansermet, *J. Magn. Magn. Mater.* **151**, 388 (1995)

[127] J.-E. Wegrowe, A. Fabian, Ph. Guittienne, X. Hoffer, D. Kelly, J.-Ph. Ansermet and E. Olive, *Appl. Phys. Lett.* **80**, 3775 (2002)

[128] A. Fabian, C. Terrier, S. Serrano Guisan, X. Hoffer, M. Dubey, L. Gravier, J.-Ph. Ansermet and J.-E. Wegrowe, *Phys. Rev. Lett.* **91**, 257209-1(2003)

[129] C. A. Foss Jr., G. L. Hornyak, J. A. Stockert and C. R. Martin, *J. Phys. Chem.* **98**, 2963 (1994)

[130] C. Schonenberger, B. M. I. Van der Zande, L. G. J. Fokkink, M. Henny, C. Schmid, M. Kruger, A. Bachtold, R. Hubber, H. Birk and U. Staufer. *J. Phys.Chem. B.* **101**, 5497 (1997)

[131] R. J. Tonucci, B. L. Justus, A. J. Campillo and C. E. Ford, *Science.* **258**, 783 (1992)

[132] H. Masuda and A. Fukuda, *Science* **268**, 1466 (1995)

[133] A. J. Yin, J. Li, W. Jian, A. J. Bennett and J. M. Xu, *Appl. Phys. Lett.* **79**, 1039 (2001)

[134] Gopal K. Mor, Karthik Shankar, Maggie Paulose, Oomman K. Varghese and Craig A. Grimes, *Nano. Lett.* **5**, 19 (2001)

[135] K. Nielsch, J. Choi, K. Schwirn, R. B. Wehrspohn and U. Gösele, *Nano. Lett.* **2**, 677 (2002)

[136] A. Kazadi Mukenga Bantu, J. Rivas, G. Zaragoza, M. A. Lopez-Quintela and M. C. Blanco, *J. Appl. Phys.* **89**, 3393(2001)

[137] A. Fert and L. Piraux, *J. Magn. Magn. Mater.* **200**, 338 (1999)

[138] J.-E. Wegrowe, *Phys. Rev B.* **68**, 214414 (2003)

[139] S. Zhao, K. Chan, A. Yelon and T. Veres*, Nanotechnology.* **18**, 245304 (2007)

국문요약

생체 분자를 검출하기 위한 나노포어와 나노구조체

장영욱

 최근 일정한 농도를 가지는 이온 용액 안에 DNA를 비롯한 생체 분자를 수 nm 크기의 작은 구멍을 가지는 나노구조체를 통과할 때 이온 전류 값의 변화를 측정하는 것으로 생체분자의 크기 혹은 길이 등을 구분하는 방법이 연구되고 있다. 특히 DNA의 경우에는 이러한 translocation 현상을 이용하여 초고속 저비용의 DNA sequencing 그리고 단백질과 같은 생체 분자는 이온 용액 내의 조건에 따른 응집 여부 및 분자의 charge 등을 예측 가능하게 해주는데 매우 유용한 기술로 사용될 것으로 기대가 되고 있다. 본 논문에서는 나노 포어를 사용하여 작은 생체 분자의 translocation을 실험적으로 관찰하고 얻어진 결과로 통계적인 해석을 진행하였다. 세부적으로 이 논문의 첫 부분에서는 나노 포어를 사용하여 DNA 의 translocation을 관찰하는 실험적인 조건과 현상에 대한 데이터 해석에 대해 다루고 두 번째 부분에서는 기존의 나노 포어 보다 쉽게 제작 가능한 수 십 nm 크기의 구멍을 가진 nanocapillary의 제작 방법과 이를 이용한 생체 분자들의 translocation 현상을

관찰하였다. 그 다음으로는 탄소 나노튜브를 이용한 가스센서를 제작하여 다양한 기체 분자의 검출과 제작한 가스센서의 탈·흡착에 대한 연구를 진행하였으며 AAO 템플레이트를 제작하고 이를 이용하여 전기도금법을 사용하여 Co/Cu와 Co/Pt 다층 나노 와이어를 제작하고 이것의 특성을 연구하였다.

핵심어: 나노포어, nanocapillary, DNA, 단백질, translocation, 탄소 나노튜브, 가스센서, 자기저항, 다층 자성 나노와이어.